Cerebellum and Plasma Metabolomics Identify Sepsis Biomarkers and MSC-sEV-Mediated Rescue

Dylan W. Crawford[1,2], Maria Triantafyllou[2], Nora Wolff[2], Marc Carlson[3], Chad Byrd[2], David R. Graham[4], Panagiotis Kratimenos[2,5,6], Vittorio Gallo[1,2,5,8,†], and Ioannis Koutroulis[2,5,9,*]

[1]Norcliffe Foundation Center for Integrative Brain Research, Seattle Children's Research Institute, Seattle, WA 98101

[2]Sheikh Zayed Institute for Surgical Innovation, Children's National Research Institute, Washington, DC 20010

[3]Research Scientific Computing, Seattle Children's Research Institute, Seattle, WA 98101

[4]Graham Scientific, LLC, Germantown, MD, 20876

[5]The George Washington University School of Medicine and Health Sciences, Washington, DC 20052

[6]Department of Pediatrics, Division of Emergency Medicine, Children's National Hospital, Washington, DC 20010

[7]Department of Pediatrics, Division of Neonatology, Children's National Hospital, Washington, DC 20010

[8]University of Washington School of Medicine, Seattle, WA, 98195

[9]Department of Pediatrics, Division of Emergency Medicine, Children's National Hospital, Washington, DC 20010

Corresponding authors:

* IKOUTROULI@childrensnational.org

† Vittorio.Gallo@seattlechildrens.org

ABSTRACT

Septic encephalopathy (SE) is a devastating complication of sepsis, marked by neuroinflammation and metabolic dysfunction, with the cerebellum being among the most affected brain regions. Progress in the field has been hindered by the incomplete characterization of cerebellar metabolic disruption in SE, a limited understanding of the therapeutic mechanisms of mesenchymal stem cell (MSC)-derived small extracellular vesicle (sEV) treatment, and the absence of reliable biomarkers for detecting SE. To address these gaps, we employed a murine sepsis model and performed metabolomic analyses of cerebellar tissue and plasma with and without MSC-sEV treatment. Sepsis induced profound cerebellar metabolic dysfunction, suppression of oxidative energy metabolism, and redox imbalance. MSC-sEVs mitigated these effects through their bioactive cargo, restoring cellular energetics and rebalancing antioxidant pathways. Cross-compartment analyses identified six plasma metabolites with strong diagnostic potential. These findings define key cerebellar metabolic mechanisms of SE and MSC-sEV treatment and propose plasma biomarkers for SE diagnostics.

INTRODUCTION

Sepsis is a major global health concern responsible for up to 20% of deaths worldwide[1] while disproportionately affecting children and underserved populations[2]. It arises from a dysregulated host response to infection marked by an imbalance between a hyperimmune response and immunoparalysis[1, 3]. One major consequence is septic encephalopathy (SE), a condition marked by neuroinflammation and metabolic disturbances in the brain[4, 5] that can result in a range of central nervous system (CNS) impairments, including cognitive and motor impairments in survivors. Previous reports have demonstrated that the cerebellum is particularly susceptible to damage through immune-mediated neuroinflammation alongside neuronal cell death resulting from SE[4]. Several studies, including our recently published work[5], have also described sepsis-associated energy deficit as a contributing factor to cerebellar and overall brain dysfunction that is ubiquitously characteristic of SE[6].

Sepsis has been shown to shift cellular energy production from efficient mitochondrial oxidative phosphorylation (OXPHOS) to energy-inefficient glycolysis[7]. Over time, cellular energy deficiencies driven by reduction in ATP production can lead to cell death and organ failure stemming from the accumulation of reactive oxygen species (ROS), oxidative stress, and apoptosis[8]. Recent evidence suggests that these energy deficits play a causal role in activating immune-mediated neuroinflammation and apoptosis in the brain[9, 10], although the full extent of the relationship between sepsis-related immunometabolic dysfunction and SE pathophysiology is not yet well understood.

The search for sepsis treatments that address deficits in both immune function and energetics has yielded limited results, with the exception of recent findings using a broad-scope, dual-therapeutic treatment targeting immune and metabolic pathways: adipose tissue mesenchymal stem cell (MSC)-derived small extracellular vesicles (sEVs). In a murine model of acute sepsis[5], as well as other sepsis-related conditions such as acute respiratory distress syndrome and bacterial pneumonia[11], MSC-sEVs have been shown to provide beneficial effects on immunometabolism. These studies confirm the significance of immune and metabolic responses in sepsis-related mortality and symptomology, as well as highlight potential therapeutic options that warrant

further investigation. Of note, our previous work demonstrates that administration of MSC-sEVs reduces SE clinical severity, partially restores aerobic metabolism, and lowers pro-inflammatory cytokines in the cerebellum[5]. However, key questions remain about the mechanisms of injury, as well as the roles of specific biological pathways and molecules that could serve as clinically relevant biomarkers.

MSC-sEVs exert their therapeutic effects primarily by way of their bioactive cargo, including microRNAs (miRNAs; including miR-21, miR-146a-5p, and miR-199a, which have established associations with improved outcomes in sepsis[12, 13]) and proteins (including Annexin A1, ATP6V1A and valosin-containing protein [VCP]). Other MSC-sEV miRNAs, including miR-30, Let-7, miR-15, and miR-338, directly control mitochondrial dynamics and OXPHOS or alter pathways to maintain lipid metabolism homeostasis, in the case of miR-30[11, 14-17]. This knowledge, coupled with the discovery that these cargo are present in abundance in MSC sEVs and activated in cerebellar tissue of treated mice[5], lend us a valuable set of high likelihood drivers of MSC-sEV mechanisms to explore.

Metabolomics techniques allow for the quantification of metabolites within biological systems and exploration of their relationships to pathophysiological states and responses to treatments of those states[18, 19]. As sepsis drives cellular energy imbalance and shifts metabolic pathways, metabolomic analysis can serve as a valuable tool for the identification of metabolic fingerprints associated with cellular adaptations experienced during sepsis. Similarly, as treatments aimed at restoring cellular energetic stability are developed, metabolomic analysis can help identify the specific metabolites involved in this recovery process. By capturing a comprehensive view of endogenous metabolites, metabolomics offers insights into the gene activity, enzymatic function, and physiological status of an organism at the time of sample collection, providing a more detailed snapshot of metabolism than conventional biomarkers[20, 21]. This robust analytical framework is thus well-suited for identifying potential biomarkers and therapeutic targets that could improve the diagnosis, prognosis, and treatment of sepsis-related conditions. Many published metabolomics studies in sepsis have focused solely on diffuse biological compartments such as plasma or urine, limiting the ability to uncover metabolic signatures of specific organs (e.g., the brain) or organ regions (e.g., cerebellum) affected by sepsis. Characterization of organ-

related metabolic biomarkers that are also present in those diffuse biological compartments could allow for minimally invasive correlational evidence of organ-related disruption early in the process, having major implications for diagnostic strategies.

Despite the advances cited above, three major gaps in knowledge remain: (1) a comprehensive characterization of metabolic disruption in SE has not been described, (2) mechanisms through which MSC-sEV treatment restores metabolic function remain unclear, and (3) reliable diagnostic biomarkers of cerebellar injury that can be detected in plasma are lacking, limiting the opportunities for early clinical intervention. In the present study, we are the first to address these key gaps by applying both targeted and untargeted metabolomic analyses to assess cerebellar tissue and plasma samples from a polymicrobial cecal slurry murine model of sepsis. First, we characterize the unique metabolomic signatures associated with acute sepsis in cerebellar tissue. Second, we assess how MSC-sEV treatment influences these profiles, integrating these findings with our existing knowledge of MSC-sEV cargo to propose potential mechanistic pathways underlying the treatment. Finally, we compare metabolomic responses associated with SE across biological compartments and identify metabolite biomarkers with strong diagnostic potential to support early SE detection and timely clinical intervention efforts. Our study employs state-of-the-art metabolomics and bioinformatics analyses of both tissue and plasma samples across biological compartments to reveal key biochemical pathways involved in disease progression and treatment response. In parallel, we identify novel metabolic biomarkers that are not only mechanistically informative, but also clinically relevant for the diagnosis, monitoring, and potential stratification of SE patients.

MATERIALS AND METHODS

Subjects

A total of 62 wildtype C57BL/6 male mice (Charles River Laboratories, strain code: 027 for cerebellum and Jackson Laboratories strain code: 000664 for plasma) aged 8-12 weeks served as the experimental subjects.

Age-matched wildtype C57BL/6 male mice served as donor animals for cecal slurry preparation. All mice were maintained in the animal facility of the Children's National Hospital and handled in accordance with the Institutional Animal Care and Use Committee (IACUC #00030714) of Children's National Hospital, who approved all the protocols and the Guide for the Care and Use of Laboratory Animals (National Institute of Health). All mice were maintained in the animal facility under a 12-hour dark-light cycle, consistent temperature (20-26 °C) and humidity (40-60%), and *ad libitum* access to food and water.

Sepsis induction via intraperitoneal cecal slurry intraperitoneal injection and MSC-sEV treatment administration via intravenous injection

Polymicrobial sepsis was induced using a well-established and extensively studied protocol[22] commonly used in our laboratories[5]. This model was chosen for its high level of reproducibility and ability to closely model the pathophysiology observed in human sepsis cases while avoiding additional undue surgical trauma or tissue damage concerns stemming from alternative methods such as traditional cecal ligation and puncture models[23]. Donor mice were euthanized and cecal contents were extracted and diluted with 5% dextrose to produce a cecal slurry with a concentration of 80 mg cecal contents/mL. Experimental mice then received an intraperitoneal (IP) injection of cecal slurry at a dose of 0.9 mg/g body weight, while controls received equivalent volume of phosphate-buffered saline (PBS).

Following a six-hour cecal slurry incubation period, a single dose of human adipose tissue MSC-derived sEVs or sEV-depleted media (used for MSC culture) was administered intravenously via lateral tail vein injection[5]. MSC-sEVs were prepared at a concentration of 10E+08 to 10E+09 particles in 250 µL by Zen-Bio (Durham, NC).

Experimental design

Experimental mice were randomly assigned to one of four groups, as previously described[5] (see **Figure 1a**):

1. **Control (-)** mice received IP injection of PBS and tail vein injection of sEV-depleted media.
2. **Control (+)** mice received IP injection of PBS and tail vein injection of MSC-derived sEVs.
3. **Sepsis (-)** mice received IP injection of cecal slurry and tail vein injection of sEV-depleted media.
4. **Sepsis (+)** mice received IP injection of cecal slurry and tail vein injection of MSC-derived sEVs.

Following IP injection in-line with group assignment, all mice were subject to evaluations every two hours for the subsequent 24-hours. Evaluations included the tracking of total and CNS-specific sepsis severity progression using a validated murine sepsis severity rubric developed by Shrum et al[24]. Mice were sacrificed 24-hours post-IP injection. For ethical reasons, mice reaching a total sepsis score ≥ 15 (on a scale from 0 to 28) before the 24-hour timepoint were sacrificed immediately and, thus, excluded from the study.

Tissue and Plasma Extraction

Cerebellar tissue was harvested from 32 mice following perfusion with PBS at the time of euthanasia. Harvested tissue was stored at -80°C until submission for mass spectrometry analysis.

Whole blood was collected intracardially from 29 mice during perfusion while anesthetized with isoflurane. Blood was drawn into 200 µL microvette tubes containing potassium EDTA (Kent Scientific, Torrington, CT). Samples were centrifuged at 2000 g for 15 minutes to obtain platelet-poor plasma, which was then stored at −80°C until submission for mass spectrometry.

Briefly, tissue or plasma metabolites were extracted on ice using a biphasic solvent mix (H_20/MeOH/IPA) that included two internal standards to ensure extraction and system reproducibility. Acetonitrile was added for protein precipitation and samples were then configured and clarified supernatants were stored for subsequent analysis by LC-MS or LC-MS/MS analysis.

Targeted Metabolomics (Panel)

The targeted method includes approximately 270 endogenous molecules with selective reaction monitoring transitions generated using authentic chemical standards and retention times using QTRAP 5500 LC-MS/MS System (Sciex) operating in both positive and negative ion modes. Five microliters of the extracted supernatants from samples were injected chromatographically resolved using a Kinetex 2.6 µm (Phenomenex) column at 0.2 mL/min flow rate with a binary gradient of water and acetonitrile (both containing 0.1% formic acid). Intensities were normalized to respective internal standard area and processed using MultiQuant 3.0.3. The quality and reproducibility of LC-MS data were ensured using pooled quality control (QC) samples, National Institute of Standards and Technology (NIST) plasma samples, and blank solvent runs between sets of samples to minimize carry-over effects.

Untargeted Metabolomics

Untargeted metabolomics analysis was comprised of two complementary mass spectrometry methods, LC-MS (a single mass spectrometry analysis following physical sample separation using liquid chromatography) and LC-MS/MS (liquid chromatography-tandem mass spectrometry, with two mass spectrometry runs to select specific ions and subsequently fragment those ions).

LC-MS. The column eluent was introduced directly into a Xevo-G2-S quadrupole-time-of-flight (QTOF) mass spectrometer (Waters Corp.) by electrospray. Mass spectrometry was performed on a QTOF mass spectrometer operating in either negative or positive electrospray ionization mode. Data was acquired in Centroid mode with a 50.0 to 1200.0 m/z mass range for TOF MS scanning. Data acquisition quality was performed using pooled QC samples (see **Supplemental Figures 1 and 3**). Metabolite annotations from this method are understood to be of Level 1-2 confidence, through identification from core facility panel confirmed by reference standard (See Schymanski et al[25] for metabolomics annotation confidence guidelines).

LC-MS feature annotation. Features that were found to differ significantly between groups following detection via LC-MS analysis were subsequently subjected to LC-MS/MS analysis to obtain spectral fragmentation data to enhance the annotation of those features. Samples were again introduced into the Xevo-G2-S QTOF (Waters Corp). Mass spectrometry was performed on a QTOF mass spectrometer operating in either negative or positive electrospray ionization, this time targeting specific m/z determined to differ significantly between groups. These features were selected in the first quadrupole (Q1), fragmented in a traveling wave collision cell for collision-induced dissociation, and detected using high-resolution time-of-flight (TOF) mass spectrometry. Fragmentation spectral data were then used to prepare QC analysis comparisons (See **Supplemental Figures 2 and 4**) and to annotate the features previously determined to differ between groups. We utilized the NIST MS Search software (version 2.4) to determine the highest probability spectral match for each targeted feature. These putative annotations are probable but not confirmed by reference samples, earning a Level 3+ degree of confidence[25].

Comprehensive metabolomic profiling validity

Although untargeted metabolomics offers broad profiling capabilities, its use in CNS-focused models is often constrained by annotation uncertainty and biological ambiguity. To address this, we employed a hybrid approach, integrating untargeted discovery with targeted reanalysis to ensure biological relevance, reproducibility, and quantitative reliability. For this reanalysis we repeated our core metabolic profiling analyses using only metabolites from the high confidence targeted metabolomics panel. This included partial least squares discriminant analysis (PLS-DA), pathway analyses, upstream regulator analyses, and biomarker screening, as described below.

Multivariate modeling

For multivariate modeling, we used unsupervised principal component analysis (PCA). For clarity of presentation, we used PLS-DA, a supervised dimensionality reduction technique that incorporates known group labels to identify latent variables that best discriminate samples between experimental conditions. While this method is known to overfit data for small sample sizes, we chose this method for narrative clarity to characterize group-level differences in metabolic profiles and identify the metabolites which have the strongest discriminatory power. Analyses were completed using the MetaboAnalyst 6.0 web interface[26] and the MetaboloAnalystR 4.0 R package[27]. Features that were putatively annotated as metabolites known to be exogeneous to mice were removed from consideration.

Pathway Analyses and Upstream Regulators

To determine pathways that were most significantly affected by differences in the screened differential metabolites from previous analyses, we utilized Qiagen Ingenuity Pathway Analysis (IPA; Qiagen Inc., https://digitalinsights.qiagen.com/IPA)[28], which references its internal catalog of primary literature to determine top canonical pathways that are expected to be up- or down-regulated based on uploaded concentrations of metabolites from our samples (see Kramer et al.[28] for a full description of IPA prediction algorithms).

In considering which top canonical pathways to consider for further analysis, we determined three pathway characteristics of interest: statistical significance, pathway coverage (number of metabolites from pathway for which we had measurements), and whether directionality of pathway regulation could be determined. Accordingly, we established a metric that we called "Pathway Impact" that incorporates these three characteristics, along with weights for each characteristic, as follows: $Pathway\ Impact = w^1 \cdot Normalized\ Significance + w^2 \cdot Pathway\ Coverage + w^3 \cdot Directionality\ Score$. "Normalized Significance" was normalized to a range of [0,1] by dividing each pathway's -log(p-value) by the maximum observed -log(p-value) across all values, "Pathway Coverage" was reported as a ratio between [0,1] (where

"zero" reflects no available measurements for metabolites from the pathway and "one" reflects all known metabolites from the pathway measured), and "Directionality Score" was a binary score based on the availability of directionality information (up- or down-regulation; 0 = no direction information, 1 = known directionality). Finally, we applied labels to impact scores, "+" or "-", which represent predicted up- or down-regulation, respectively. For this study, weights of 0.5, 0.3, and 0.2 were used for "Normalized Significance", "Pathway Coverage", and "Directionality Score", respectively.

Comparison of the Sepsis (-) v. Control (-) groups served to assess the disease state condition, Sepsis (+) v. Sepsis (-) as the treatment state condition, and the four remaining comparisons (Control (+) v. Control (-), Sepsis (-) v. Control (+), Sepsis (+) v. Control (-), Sepsis (+) v. Control (+)) served as subordinate supplemental comparisons. We also considered the top 10 identified differences between conditions in upstream regulators as determined by absolute value of their activation z-score (i.e., those regulators that were projected to be influenced the most by condition) using Qiagen IPA's Upstream Regulator Analysis.

Biomarker candidate selection and evaluation

Metabolites were evaluated on their capacity for discriminating animals between Sepsis (-) and Control (-) conditions based on concentration levels in both cerebellar tissue and plasma. Receiver operating characteristic (ROC) curves were generated using MetaboAnalyst 6.0[26] and MetaboAnalystR[27] to evaluate and visualize sensitivity-specificity trade-offs for individual metabolites. Biomarker viability was evaluated using models' area under the ROC curve (AUC) as a measure of the metabolite's ability to distinguish between Sepsis (-) and Control (-) groups. Metabolites with AUC values ≥ 0.8 and < 0.9 have considerable diagnostic performance and those with AUC values ≥ 0.9 have excellent performance[29]. In line with these criteria interpretations, endogenous metabolites with AUC values ≥ 0.8 were considered as biomarker candidates.

RESULTS

Cecal slurry injection induced acute sepsis and SE with clinical recovery following MSC-sEV treatment

A total of 61 animals ($n_{Control\ (-)} = 16$, $n_{Control\ (+)} = 15$, $n_{Sepsis\ (-)} = 15$, $n_{Sepsis\ (+)} = 15$) were evaluated using the aforementioned validated murine sepsis severity rubric[24] (**Figure 1b**). Following a one-way ANOVA comparing average total sepsis scores at the time of treatment injection ($F_{(3,57)} = 61.18$, $p < 0.001$), Tukey's HSD post-hoc analysis revealed no significant difference between Sepsis (+) and Sepsis (-) groups ($M_{Sepsis\ (+)} = 3.93$, $M_{Sepsis\ (-)} = 3.00$, $p = 0.07$). In considering average peak total sepsis scores during observations (i.e., highest sepsis score throughout the 24-hour observation period), we found a significant main effect of condition ($F_{(3,57)} = 253.05$, $p < 0.001$), characterized by a significant decrease in septic mice treated with MSC-sEVs relative to untreated mice ($M_{Sepsis\ (+)} = 11.13$, $M_{Sepsis\ (-)} = 12.87$, $p = 0.03$) according to post-hoc analyses. Despite a significant main effect in the average total sepsis scores between sepsis groups at the time of sacrifice as determined by one-way ANOVA ($F_{(3,57)} = 125.40$, $p < 0.001$), Tukey's HSD post-hoc analysis found no significant difference between sepsis groups ($M_{Sepsis\ (+)} = 10.13$, $M_{Sepsis\ (-)} = 11.47$, $p = 0.35$). At each of the three points of measurement described above, both sepsis groups scored significantly higher relative to both control groups ($p < 0.001$ for each comparison), while there was no significant difference between Control (-) and Control (+) groups ($p_{Injection} = 1.0$, $p_{Peak} = 0.99$, $p_{Sacrifice} = 1.0$).

We also considered a subset of the total sepsis scores previously reported[5] to assess CNS-related function (i.e., level of consciousness, general activity, and response to stimuli; **Figure 1c**). In addition to a significant main effect of condition as determined by one-way ANOVA ($F_{(3, 57)} = 49.26$, $p < 0.001$), Tukey's HSD post-hoc analysis comparing average CNS-related sepsis scores at the time of treatment injection revealed that mice in the Sepsis (+) group had a significantly higher average CNS-related sepsis score at the time of treatment injection relative to mice in the Sepsis (-) group ($M_{Sepsis\ (+)} = 2.73$, $M_{Sepsis\ (-)} = 1.93$, $p = 0.03$). Following a significant one-way ANOVA considering average CNS-related peak scores ($F_{(3,57)} = 283.57$, $p < 0.001$), Tukey's HSD post-hoc analysis determined that there was a significant decrease of CNS-related peak

scores in the group treated with MSC-sEVs relative to non-treated animals ($M_{Sepsis\ (+)} = 6.47$, $M_{Sepsis\ (-)} = 7.67$, $p = 0.005$). While there was an overall main effect of condition on average CNS-related sepsis scores at the time of sacrifice between groups ($F_{(3,57)} = 161.08$, $p < 0.001$), post-hoc analysis revealed no significant difference between sepsis groups at the time of sacrifice ($M_{Sepsis\ (+)} = 5.87$, $M_{Sepsis\ (-)} = 6.93$, $p = 0.06$). At each of the three points of measurement described above, both sepsis groups had significantly higher scores relative to control groups ($p < 0.001$ for each comparison), while there was no significant difference between Control (+) and Control (-) groups ($p_{Injection} = 1.0$, $p_{Peak} = 0.98$, $p_{Sacrifice} = 1.0$).

These clinical observations were consistent with our previously published findings, confirming the successful induction of acute sepsis and mitigation of both systemic and CNS-specific severity following MSC-sEV treatment under the same experimental conditions[5]. Building on our prior evidence of cerebellar vulnerability in this model, the current findings support a cerebellum-focused metabolomic analyses to investigate the underlying mechanisms of injury and MSC-sEV-mediated recovery.

Metabolic profiling revealed distinct cerebellar and plasma signatures in sepsis and treatment

The feature detection process was applied to both cerebellar tissue and plasma samples to identify and annotate as many features/metabolites as possible (see **Supplemental Table 1** for a summary). Using untargeted LC-MS, we detected 9550 features in cerebellar tissue, including 4024 in NEG ionization mode and 5526 in POS ionization mode. In plasma samples, 10,366 features were detected (5187 NEG and 5179 POS). Of these detected features, 463 in cerebellar tissue and 671 in plasma samples differed significantly in concentration between groups. Importantly, these represent raw spectral features, many of which are not directly interpretable as known metabolites.

Samples were re-injected and tandem MS was performed on features previously identified as significant, using targeted retention time and m/z windows for collision-induced dissociation (CID). Following LC-MS/MS analysis, fragmentation spectra were compared with spectral libraries using the NIST MS Search 2.4 tool which

allowed for the putative annotation of 174 metabolites from cerebellar tissue and 373 metabolites from plasma samples. Combined with the 324 known metabolites from the metabolite panel (previously annotated), a total of 498 metabolites in cerebellar tissue and 697 in plasma samples were annotated and quantified for use in all subsequent downstream analyses.

Cerebellar metabolomic signatures reflected both disease and treatment effects, while plasma profiles were driven by disease status alone

Maps of the first two components identified by PLS-DA modeling of cerebellar tissue results are shown in **Figure 2a**, where within-group samples are generally shown to cluster together (shaded ovals represent a 95% confidence interval). Component 1 explained 18.7% of the variance in the metabolite data matrix (X), which consists of the relative abundances of metabolites across all samples and captured the strongest direction of group separation. Component 2 explained 21.4% of the X variance and represented a secondary, orthogonal pattern that also contributed to group separation. Although Component 2 captured more of the total variance in metabolite concentrations across all samples, Component 1 was assigned as such because it more closely aligned with group labels, consistent with the goal of PLS-DA in maximizing the covariance between predictors (X) and group membership (Y). An analogous PCA plot showing the unsupervised separation between groups can be found in **Supplemental Figure 5a.**

Using 5-fold cross validation, we found that the model performed best with four group comparisons, yielding an average classification accuracy of 0.608, R^2 of 0.790, and Q^2 of 0.777, indicating strong performance with high explained variance and predictive capability. Notably, each of the four experimental groups forms a partially distinct cluster, suggesting the cerebellar metabolic profile is sensitive to both disease and treatment effects. We also obtained variable impact importance in projection (VIP) scores from Component 1, which quantify each metabolite's weighted contribution to the model's discriminative power (the top 10 metabolites by VIP score and their relative concentrations in each group are displayed in **Figure 2b**). Relative

concentrations of these top 10 metabolites for individual samples are displayed in the heatmap found in **Figure 2c**.

In contrast to cerebellum, a PLS-DA model of plasma samples revealed clear separation between control and sepsis groups with limited separation based on treatment (i.e., Control (-) and Control (+) groups clustered together, as did Sepsis (-) and Sepsis (+) groups; see **Figure 2d**). This lack of treatment-associated separation in plasma, in stark contrast to the distinct treatment effects observed in cerebellar tissue, suggests that MSC-sEV treatment impact was localized rather than systemic. Component 1 explained 38.9% of the variance in the metabolite data matrix while Component 2 explained 20.8%. The PLS-DA was optimized with two group comparisons, yielding an average classification accuracy of 0.412, R^2 of 0.613, and Q^2 of 0.538, indicating moderate separation with acceptable predictive capacity. Top 10 metabolites by VIP score and their relative concentrations are shown in **Figure 2e**. Relative concentrations of these top 10 metabolites for individual samples are displayed in the heatmap found in **Figure 2f**. See **Supplemental Figure 5b** for a PCA plot of these groups.

Cumulatively, these results illustrated that cerebellar metabolic profiles were influenced by both disease state and treatment conditions, while plasma profiles were primarily influenced by disease state condition alone. Having established global metabolomic patterns across cerebellar tissue and plasma, we next focused exclusively on cerebellar tissue to isolate sepsis- and treatment-induced metabolic changes specifically in this brain region.

Cerebellar metabolomic profiling revealed metabolic dysfunction, suppression of oxidative energy metabolism, and redox imbalance in SE

To characterize metabolic alterations associated with SE, we applied an integrated metabolic analysis combining PLS-DA modeling, pathway enrichment, and upstream regulator prediction using annotated and

quantified metabolites from cerebellar tissue. The following results identify key metabolites, canonical pathways, and upstream regulators driving changes across septic and control conditions.

Isolating disease state, we identified a PLS-DA model with strong separation between groups (**Figure 3a**) where Component 1 explains 13.3% of the variance in the metabolite data matrix and Component 2 explains 28.6%. This model was optimized for two groups, resulting in an average classification accuracy of 0.817, R^2 of 0.886, and Q^2 of 0.474. We then identified the top 10 metabolites driving differences between groups using metabolite VIP scores (ranging from 2.15 – 4.22 for these top 10 features; see **Figure 3b**). Identified metabolites include *N-oleoglycine, ^Spermine, ^Spermidine, ^Dopamine, ^Hypoxanthine, ^Putrescine, ^1-methyl-L-histidine, ^3-hydroxyl-3-methylglutaryl-COA, ^Glucosamine, and ^Guanosine. All metabolites with the exceptions of ^Dopamine and ^Hypoxanthine were increased in the septic group relative to controls (see **Figure 3c-l**; ^ Denotes a Level 1-2 confidence identification from core facility panel confirmed by reference standard; * Denotes a putatively annotated feature from LC-MS/MS fragmentation matches using the NIST MS Search software, earning Level 3+ identification confidence[25]). A PCA plot of this comparison can be found in **Supplemental Figure 6a.**

Pathway analyses resulted in a total of 904 canonical pathways predicted to be altered between septic and non-septic conditions. **Figures 4a** displays all pathways predicted to be altered between disease states. Each bubble represents an altered pathway and is grouped based on biological function (y-axis). We further explored the nature of the top 20 pathways (illustrated in **Figure 4b**) as determined by Pathway Impact score (see **Supplemental Figures 7-10** and **Supplemental Table 2** for data from additional comparisons).

We identified the top 20 affected pathways and grouped them into eight categories based on their overall biological functions, listed in order of descending impact: metabolism, transport of small molecules, intracellular and secondary messenger signaling, transcription regulation, biosynthesis, degradation/utilization/assimilation, autophagy, and DNA repair (**Figure 4b**, see **Table 1** for a complete list of top 20 pathways, their biological function category, and Pathway Impact score). The five most significantly

impacted pathways included nucleotide catabolism, transport of bile salts and organic acids, metal ions and amine compounds, superpathway of citrulline metabolism, urea cycle, and arginine biosynthesis IV.

We further found that the upstream regulators CA9, SIRT5, EP300, adenine, CUEDC2, ALDH2, L-glucose, CSF3, APOA1, and immunoglobulin were the most influenced regulators. All regulators were down-regulated in septic animal relative to controls, with the exceptions of SIRT5 and adenine which were up-regulated (see **Figure 4c**).

Changes at the metabolites, pathways, and regulator networks following sepsis induction revealed widespread metabolic dysfunction in the cerebellum. Findings suggested disruptions in nucleotide turnover, oxidative energy metabolism, and redox balance. The culmination of these disruptions established a baseline against which the metabolic mechanisms of MSC-sEV treatment cerebellar injury mitigation were assessed.

MSC-sEV treatment partially reversed sepsis-induced cerebellar metabolic disruptions

We next applied the same integrated metabolic profiling procedure using PLS-DA, pathway analysis, and upstream regulator prediction to cerebellar tissue of MSC-sEV-treated septic mice compared to untreated. The following results identify treatment-associated changes in metabolite levels, canonical pathways, and predicted upstream regulators between MSC-sEV-treated and untreated septic animals.

We identified an effective prediction model constructed by way of PLS-DA, where Component 1 explains 23.7% of the variance in the metabolite data matrix and Component 2 explains 26.9% (**Figure 3m**). This model was optimized with 2 components, resulting in an accuracy measure of 0.75, an R^2 value of 0.779, and a Q^2 value of 0.399. The top 10 metabolites driving differences between groups were then identified (VIP scores ranging from 2.15 – 2.98; see **Figure 3n**) as ^Glycerophosphocholine, *Glutathione, *Oxiglutathione, *D-Ribulose 5-phosphate, *N-oleoglycine, ^Citicoline, ^Pyrophosphate, ^Uridine Diphosphate Glucose, ^Spermine, and ^Uridine 5-diphosphate. Each of these metabolites were lower in concentration in MSC-sEV

treated animals relative to untreated animals (see **Figure 3o-x**). A PCA plot from this comparison can be found in **Supplemental Figure 6b**.

Pathway analysis identified a total of 904 impacted pathways (**Figure 4d**). Notably, the top 20 pathways fell into the same eight biological function categories previously found to be influenced by sepsis: transport of small molecules, biosynthesis, metabolism, intracellular and secondary messenger signaling, transcriptional regulation, degradation/utilization/assimilation, autophagy, and DNA repair (**Figure 4e, Table 1**). The top five most influenced pathways as determined by Pathway Impact score were determined to be transport of bile salts and organic acids, metal ions and amine compounds, superpathway of citrulline metabolism, urea cycle, arginine biosynthesis IV, and citric acid cycle (tricarboxylic acid [TCA] cycle).

Analysis of upstream regulators in cerebellar tissue identified the top 10 most influential regulators, which included CA9, GAPDH, OGT, EP300, GATA4, SIRT2, ERBB2, HIF-1α, CUEDC2, and PRKAA1. Each of the listed regulators were predicted to be up-regulated in MSC-sEV treated septic mice relative to non-treated, with the exceptions of GAPDH and OGT, which were predicted to be down-regulated (see **Figure 4f**).

In summary, alterations in the metabolic profiles of MSC-sEV treated animals revealed partially reversed sepsis-induced metabolic dysfunction in the cerebellum. Data from metabolite, pathway, and upstream regulator analyses indicated reductions in oxidative stress markers, normalization of amino acid and nucleotide metabolism, and activation of antioxidant and repair-associated regulators. These findings support a treatment model focused on restoring redox homeostasis and cellular energetics. These results also provided a foundation for evaluating the impact that specific MSC-sEV cargo may exert in driving the recovery observed in treated animals. Figures and tables generated from plasma data which are analogous to those described above from cerebellar tissue can be found in **Supplemental Figures 11 – 13** and **Supplemental Tables 3** and **4**.

Cross-compartment metabolite screening identified candidate plasma biomarkers of sepsis-associated cerebellar injury

To evaluate the potential for peripheral biomarkers of sepsis-associated cerebellar injury, we next performed cross-compartment analyses of metabolite candidates from cerebellar tissue and plasma. ROC analyses were used to assess diagnostic accuracy and efficiency of candidate metabolites in distinguishing septic from control animals. We identified metabolites with considerable (AUC values ≥ 0.8) and excellent (AUC values ≥ 0.9) diagnostic criteria[29] between septic and control animals in cerebellar tissue and plasma. Among the cerebellar metabolite candidates, we aimed to identify overlapping plasma metabolites that could serve as peripheral indicators of sepsis-associated cerebellar injury.

We found 24 metabolites with AUC values ≥ 0.8 that were considered as viable biomarker candidates from cerebellar tissue (**Supplemental Figure 14**). Of these, 16 were up-regulated in septic animals relative to controls: ^N-acetylglutamine (AUC: 0.977), *N-oleoylglycine (AUC: 0.914), ^Betaine (AUC: 0.875), ^Cystathionine (AUC: 0.875), *1-(9Z-octadecenoyl)-sn-glycero-3-phosphocholine (AUC: 0.859), *17-Oxo-4(Z),7(Z),10(Z),13(Z),15(E),19(Z)-docosahexaenoic acid (AUC: 0.844), ^L-acetylcarnitine (AUC: 0.844), *Ptdlns-(3,4,5)-P3 (1-stearoyl, 2-arachidonoyl) (AUC: 0.844), *Substance P (3-11) (AUC: 0.844), *[Ser2]-Neuromedin C (AUC: 0.836), ^1-Methyl-L-Histidine (AUC: 0.828), *Arachidonamide (AUC: 0.828), *ADP-D-Ribose (AUC: 0.828), ^Urea (AUC: 0.828), ^Putrescine (AUC: 0.812), and *N-acetyl-L-aspartic acid (AUC: 0.812). The remaining eight were decreased in septic animals relative to controls: *Amyloid beta-protein (25-35) amide (AUC: 0.953), ^Dopamine (AUC: 0.906), ^Betaine aldehyde (AUC: 0.883), *1,2-dipalmitoyl-sn-glycero-3-phosphoethanolamine (AUC: 0.875), ^Choline (AUC: 0.875), ^Dimethylglycine (AUC: 0.875), *1,2-dilinoleoylglycerol (AUC: 0.844), and Atrial natriuretic peptide (ANP, 1-28; AUC: 0.828).

In plasma, we found a total of 396 metabolites with AUC values ≥ 0.80, qualifying for biomarker consideration. Of those, 187 metabolites were decreased in septic animals relative to controls and 210 were increased in septic samples. Of the 24 biomarker candidates discovered in cerebellum, we found nine

overlapping metabolites with sufficient diagnostic power (i.e., AUC ≥ 0.8) to identify septic vs. control animals present in plasma: ^1-Methyl-L-Histidine (AUC: 1), ^Choline (AUC: 1), ^Putrescine (AUC: 1), ^Dimethylglycine (AUC: 1), ^N-Acetylglutamine (AUC: 1), ^Urea (AUC: 1), ^Cystathionine (AUC: 0.963), *N-Acetyl-L-Aspartic acid (AUC: 0.877), *1-(9Z-octadecenoyl)-sn-glycero-3-phosphocholine (AUC: 0.815; **Figure 5a-i**). While all nine metabolites were retained and displayed in **Figure 5** for meeting the specified AUC criteria, six of the nine overlapping metabolites showed consistent directionality in concentrations differences between groups (e.g., Sepsis (-) showed an increase in 1-Methyl-L-Histidine concentration relative to Control (-) in both cerebellum and plasma). The remaining three metabolites, ^Choline, ^Dimethylglycine, and *1-(9Z-octadecenoyl)-sn-glycero-3-phosphocholine, had concentration levels were inconsistent between cerebellum and plasma and were not considered biologically congruent between compartments.

Through these analyses, we identified a subset of cerebellar metabolites that not only distinguished septic animals from controls with strong diagnostic accuracy but were also detectable in plasma with similarly strong diagnostic value. These findings suggest that these metabolites may have utility as peripheral biomarkers of cerebellar injury associated with sepsis. Overlapping metabolites with consistent directionality across compartments were identified, strengthening their potential as clinically accessible indicators of CNS-specific metabolic disruption.

Confirmatory reanalysis of metabolic profiling using targeted metabolomics alone

Beginning with PLS-DA, we found consistent group separation patterns between the four experimental groups as determined by the models generated from both metabolite datasets (**Figures 2a, 2d**; **Supplemental Figures 15a, 15d;** PCA plots reported in **Supplemental Figure 16**). In cerebellum, eight of the top 10 metabolites by VIP score were consistent between both sets (**Figure 2b**; **Supplemental Figure 15b**), while three of the 10 were consistent in plasma (**Figure 2e**; **Supplemental Figure 15e**). Considering disease state- and treatment-specific comparisons in cerebellum, we again found consistent group separation in both cases (**Figures 3a, 3m**;

Supplemental Figure 17a, 17m; PCA plots reported in **Supplemental Figure 18**). Nine of the top 10 metabolites were consistent in the disease state comparison (**Figure 3b**; **Supplemental Figure 17b**), while six out of 10 were consistent in the treatment comparison (**Figure 3n**; **Supplemental Figure 17n**). See **Supplemental Figures 19**, **20** for comparable results in plasma.

Cerebellar pathways analyses between comprehensive and targeted-only metabolomic datasets resulted in consistent pathway identification and alteration directionality in 15 out of the top 20 pathways for both disease state- and treatment-specific comparisons (**Table 1**; **Supplemental Table 5**). Cerebellar upstream regulators showed strong consistency, with seven of the top 10 overlapping in the disease state comparison (**Figure 4c**; **Supplemental Figure 21c**) and eight out 10 in the treatment comparison (**Figure 4f**; **Supplemental Figure 21f**). See **Supplemental Figure 22** for comparable results in plasma.

Finally, reanalysis of cerebellar biomarker candidates using only targeted metabolomics data identified 22 metabolites satisfying our threshold criteria with AUC scores ≥ 0.8 (eight of which were consistent with the comprehensive metabolomics dataset; **Supplemental Figure 23**). Among metabolites overlapping with plasma, we identified 13 biomarker candidates, seven of which were consistent with findings from the comprehensive metabolomics dataset (**Supplemental Figure 24**).

Overall, the reanalysis showed strong agreement between the comprehensive and targeted-only datasets across multivariate modeling, pathway analysis, upstream regulator predictions, and biomarker identification. This consistency, especially in cerebellar tissue, reinforces the robustness of our core findings and supports the reliability of the identified metabolic signatures. At the same time, differences between datasets helped clarify the unique contributions of each approach to our broader interpretation of the influences of disease state and treatment.

DISCUSSION

Despite increasing recognition of the CNS's vulnerability in sepsis, the metabolic underpinnings of sepsis-associated brain injury remain poorly defined. While prior studies have highlighted inflammation and blood–brain barrier (BBB) dysfunction as contributors to SE, there is a significant knowledge gap regarding the specific metabolic alterations occurring within affected brain regions, particularly the cerebellum. Moreover, few studies have explored how systemic metabolic changes are reflected in those CNS regions or assessed how therapeutic interventions may modify these metabolic profiles. MSC-sEVs have emerged as a promising therapeutic platform due to their immunomodulatory and tissue-protective properties, yet the mechanisms by which they exert neuroprotective effects, especially at the metabolic level, remain largely undefined. Further, clinical opportunities for early intervention are limited by a lack of tissue-specific biomarkers of SE. To address these gaps, our study investigates (1) the cerebellar tissue metabolic profiles in acute polymicrobial sepsis, (2) cerebellar tissue metabolomic alterations observed following MSC-derived sEV treatment, and (3) metabolomic biomarkers of sepsis-associated injury that are detectable in both cerebellum and plasma using a murine model of acute polymicrobial sepsis.

Comprehensive profiling cerebellar metabolic signatures in septic and treated animals revealed extensive changes across a wide array of metabolites, offering insight into underlying cellular processes. These findings reveal significant disruptions in metabolic pathways within cerebellar tissue of septic mice compared to non-septic controls, indicating substantial neuro-metabolic involvement during sepsis. Importantly, treatment with MSC-sEVs notably reshaped these metabolic alterations, pointing to specific mechanistic pathways of action described below (see **Figure 6**). We propose potential mechanisms of action of MSC-sEVs through their specific miRNA and protein cargo previously identified by our group (such as members of Let-7, miR-21, and miR-30 families[5]) and how these bioactive molecules may regulate metabolic and inflammatory pathways to mitigate sepsis-associated deficits as suggested by our metabolomic findings. Additionally, our comparative analysis between cerebellum and plasma provided insights into localized versus systemic metabolite profiles during sepsis. This comparative approach enabled the identification of cerebellum-specific metabolites with

strong diagnostic potential in plasma, laying the groundwork for early, non-invasive detection of sepsis-associated brain injury.

Sepsis was associated with dysregulated nucleotide metabolism, including elevated levels of guanosine and adenine. This coincided with increased activation of the purine nucleotide de novo biosynthesis pathway, suggesting that cerebellar cells may be attempting to augment purine nucleotide production[30] in response to stress or increased turnover. However, concurrent downregulation of the interconversion of nucleotide di- and triphosphates and overall nucleotide biosynthesis pathways suggest a bottleneck in converting intermediates into fully functional high-energy nucleotides such as ATP and GTP. This likely impairs both cellular energy homeostasis and nucleic acid synthesis. MSC-sEV treatment reversed these effects by up-regulating NDP ⇄ NTP interconversion and basal nucleotide biosynthesis, while suppressing nucleotide salvage and purine nucleotides de novo biosynthesis II pathways. These changes suggest a shift away from compensatory production routes toward restored homeostatic balance. Reductions in intermediate metabolites such as D-ribulose-5-phosphate and pyrophosphate further imply decreased flux through pathways typically activated under cellular stress conditions. These restorative effects may be partially mediated by MSC-sEV cargo proteins ATP6V1A[31] and VCP[31], which have been shown to regulate ATP-generating metabolic pathways and mitochondrial function[32], thereby supporting improved nucleotide metabolism and energy homeostasis.

Sepsis impaired membrane transport and remodeling, as evidenced by down-regulations of APOA1, along with suppression of the transport of bile salts and organic acids, metal ions, and amine compounds pathway, and the choline catabolism pathway. These alterations are hallmarks of defective lipid clearance, detoxification, and phospholipid turnover that likely compromise membrane integrity and synaptic signaling. Following MSC-sEV treatment, we observed an upregulation of CUEDC2 expression which may suggest enhanced regulatory control over membrane-associated inflammatory responses. Additionally, the reactivation of transport pathways indicates an improved capacity for transmembrane movement of key metabolites and ions. Upregulation of the choline catabolism pathway following MSC-sEV treatment may reflect increased choline turnover to support membrane phospholipid remodeling. Notably, MSC-sEV cargo protein Annexin A1

may contribute to the modulation of membrane-associated inflammation[33, 34], potentially acting in concert with CUEDC2 to regulate inflammatory responses. Concurrent decreases in glycerophosphocholine and citicoline[35] may indicate reduced demand for acute membrane repair mechanisms.

With regard to nitrogen and amino metabolism, a pronounced shift towards hypercatabolism was evident in septic metabolic profiles. We found that concentrations of polyamines and 1-methyl-L-histidine were increased, alongside up-regulations of urea cycle, arginine biosynthesis IV, and citrulline-nitric oxide (NO) cycle pathways. These results suggest increased synthesis of NO, a key mediator of inflammatory and vasodilatory responses commonly implicated in sepsis pathogenesis. Up-regulation of the super pathway of methionine degradation indicates an increased breakdown of methionine[36], contributing further to the catabolic state of septic cerebellar tissue. In parallel, a decrease in dopamine accompanied prediction down-regulation of CUEDC2[37], sulfur amino acid metabolism, and glutamate/glutamine metabolism pathways, reflecting a potentially compromised antioxidant defense, while simultaneously reducing the substrates needed for anabolic processes or efficient energy transfer. MSC-sEV treatment appears to have rebalanced these processes via GATA4-driven transcriptional activation[38] and up-regulating sulfur amino acid and glutamate/glutamine metabolism pathways to preserve glutathione, optimize nitrogen handling, and limit polyamine accumulation, urea cycle flux, arginine/NO production, and methionine degradation. The balanced inflammatory response associated with MSC-sEV treatment could be attributable to the actions of cargo such as miR-146 and miR-199a, known regulators of TNF-α, IL-6, and NF- κB signaling[13, 39, 40], as well as protein Annexin A1[33, 34].

Core energy and carbon metabolism pathways were severely impaired during sepsis. Marked downregulation of the TCA cycle and pyruvate metabolism pathways, accompanied by reduced availability of L-glucose, provides strong evidence that central pathways for ATP production and carbon utilization were compromised. Concurrent increases in intermediate metabolites such as N-oleoylglycine, 3-hydroxy-3-methylglutaryl-CoA, glucosamine, and adenine could suggest compensatory efforts via alternative substrates to sustain energy production and cell viability. MSC-sEVs reversed these deficits by up-regulating HIF-1α[41] to defend the cell against oxidative damage by decreasing the OXPHOS and mitochondrial ROS production[42].

AMP-activated protein kinase (AMPK; evidenced through subunit PRKAA1) was also up-regulated, driving mitochondrial biogenesis[43] and mitophagy[42] and resulting in a net increase in healthy cellular mitochondria. Here, another subset of MSC-sEV cargo, miR-30, Let-7, and miR-26, are likely to be responsible for these ameliorations on mitochondrial energetics and metabolic pathways, as they have all been shown to regulate mitochondrial dynamics and OXPHOS (with miR-30 also altering metabolic pathways to maintain lipid metabolism homeostasis)[11, 14-17, 44]. Cargo proteins ATP6V1A and VCP have also been associated with the regulation of ATP-generating pathways[31, 32], with VCP also shown to support mitochondrial respiration[32]. Predicted up-regulation of receptor kinase ERBB2 can drive activation of the PI3K/AKT signaling pathway, which serves to further up-regulate H1F-1α transcription[45-47]. These changes restored TCA cycle, pyruvate metabolism, and glyoxylate metabolism/glycine degradation. Down-regulation of N-oleoylglycine and GAPDH[48] thereby attenuates TNF-α production and suppresses the gluconeogenesis I pathway, indicating that cells are no longer relying on emergency glucose production following the administration of the MSC-sEV treatment. Given that hyperglycemia is a frequent and clinically-concerning metabolic derangement observed in septic patients[49, 50], this down-regulation may be indicative of a return to a basal gluconeogenesis state.

Redox homeostasis and co-factor metabolism were also impaired in sepsis. Key protective and regulatory elements, including EP300, CA9, ALDH2, and the sirtuin signaling cycle, were all downregulated in septic animals relative to controls. These components are critical for mounting an effective antioxidant response and maintaining redox balance[51, 52]. We also found a predicted up-regulation of the metabolism of water-soluble vitamins and cofactors and flavin biosynthesis IV pathways. Water-soluble vitamins, such as vitamins B and C, are essential for enzymatic reactions involved in energy metabolism, redox balance, and antioxidant defense which have shown promising potential as therapeutic targets for sepsis treatment in recent years[53]. Flavins, synthesized through the flavin biosynthesis IV pathway, function as critical cofactors (FAD and FMN) for various redox reactions within the mitochondria and cytoplasm, significantly influencing cellular energy production and antioxidant defense mechanisms[54]. Up-regulation of these pathways could reflect a compensatory response to severe oxidative stress and cellular damage. Notably, the SIRT5 upstream regulator

was up-regulated in septic animals, in contrast to the above expected biological output and a recently published report[55]. This paradoxical increase may reflect a compensatory cellular response aimed at counteracting severe oxidative and metabolic stress through alternative regulatory pathways; however, it remains unclear whether this up-regulation is functionally protective or simply indicative of stress-induced dysregulation. Following MSC-sEV treatment, predicted activation of EP300[56, 57] and SIRT2[58, 59] may drive transcription of antioxidant genes and deacetylation of metabolic enzymes critical for ROS detoxification. We propose a support mechanism by way of MSC-sEV cargo such as miR-21 - which is overexpressed in neutrophils and macrophages in sepsis[12] - and Let-7, providing additional reinforcement to these antioxidant defenses by attenuating oxidative stress and inflammatory signaling. Concurrent up-regulation of CA9 supports NADPH/$NADP^+$ homeostasis and glutathione reductase activity[57], while continued up-regulation of water-soluble vitamin/cofactor metabolic pathway suggests improved supply of essential vitamins and cofactors needed for redox enzymes. Glutathione[60], as well as its oxidized form oxiglutathione, was present in lower concentration in the tissue of treated mice relative to untreated, potentially indicative of alleviated oxidative burden, while down-regulation of OGT[61, 62], the sirtuin signaling cycle pathway, and the flavin biosynthesis IV pathway could reflect similar diminished requirements for emergency or compensatory antioxidant responses.

Finally, sepsis triggered activation of core DNA repair mechanisms (e.g., mismatch repair) and innate immune detection (cytosolic sensors of pathogen-associated DNA), suggesting that cells are actively responding to DNA damage and heightened oxidative stress. The septic metabolic profile also describes the downregulation of several negative or modulatory components of immune regulation (including CUEDC2, immunoglobulin, and CSF3), suggesting impaired capacity to regulate inflammatory and stress responses. This imbalance may result in prolonged inflammatory signaling, exacerbating cellular stress and potentially contributing to tissue damage or dysfunction characteristic of sepsis. MSC-sEV treatment re-established homeostasis by up-regulating CUEDC2 to initiate the cessation of inflammation. Simultaneously, down-regulation of the mismatch repair pathway suggests a reduced need for DNA repair, consistent with reduced oxidative and inflammatory stress following treatment. Overall, these results suggest that MSC-sEV treatment is alleviating the DNA damage and

inflammatory burden placed on cells by sepsis. These reductions in DNA damage responses and inflammatory signaling pathways may also reflect a specific mechanism of miRNA intervention, such as miR-146 and miR-199a, in addition to Annexin A1. Collectively, this cargo may be modulating critical inflammatory signaling cascades[13, 33, 34, 39] and reducing oxidative stress-induced DNA damage, supporting an overall decrease in cellular stress and injury.

In summary, our proposed mechanistic models (see **Table 2**) highlight how MSC-derived sEV cargo, including specific miRNAs (miR-146a, miR-199a, miR-30, Let-7, miR-26, and miR21) and proteins (Annexin A1, ATP6V1A, VCP), may regulate key metabolic, inflammatory, and stress-response pathways during sepsis. These integrated pathways align with the treatment-associated improvements observed in the cerebellum, including reductions in oxidative and inflammatory stress, restoration of mitochondrial and energy metabolism, and decreased evidence of DNA damage, as revealed by our comprehensive metabolomics analyses. While the links reported between MSC-sEV cargo and observed metabolic profile are limited to correlation in this study, these results provide preliminary support for future studies to functionally validate causal relationships.

Given these extensive disruptions to metabolic and inflammatory processes observed in cerebellar tissue, we next sought to identify peripheral SE biomarkers that could reliably reflect localized cerebellar distress and thus offer accessible, non-invasive diagnostic criteria for sepsis-associated injury. To this end, we implemented a cross-compartment screening strategy to identify plasma metabolites that reflect the metabolic signatures of sepsis-associated cerebellar distress.

We identified six metabolites (1-Methyl-L-Histidine, Putrescine, N-Acetylglutamine, Urea, Cystathionine, and N-Acetyl-L-Aspartic acid) that were elevated in both cerebellar tissue and plasma of septic animals compared to controls. Coupled with high diagnostic performance demonstrated by results from ROC curve analyses across both components, the mechanistic relevance to sepsis pathophysiology makes these metabolites strong candidates for consideration in the search for diagnostic biomarkers of sepsis-associated cerebellar damage. 1-Methyl-L-Histidine is a methylated derivative of amino acid histidine, derivatives of

which have been associated with protein degradation under septic conditions and identified as potential sepsis biomarkers from serum and urine analyses in critically-ill septic patients[63]. Putrescine is a polyamine derived from the amino acid ornithine that has been associated with increased BBB permeability and neuronal integrity during times of neuroimmune stress[64]. Its derivative, N-acetylputrescine, has previously been reported as a potential biomarker to distinguish patients with systemic inflammatory response syndrome (SIRS) or sepsis from heathy controls[65]. N-acetylglutamine is an acetylated form of the amino acid L-glutamine, a precursor of excitatory neurotransmitter glutamate. Impairments in the urea cycle during sepsis may lead to accumulations of upstream intermediates such as N-acetylglutamine, which has previously been identified as a biomarker for sepsis in a pig model[66]. Urea, a byproduct of protein metabolism, is a critical component of blood urea nitrogen SIRS levels which are commonly higher in septic patients and indicative of renal impairment[67]. Cystathionine is an important intermediate in the transsulfuration pathway, which links methionine metabolism to cysteine and glutathione synthesis and makes it an important metabolite in the maintenance of redox homeostasis. Increased concentration of cystathionine in septic animals may demonstrate an increased demand for glutathione to counteract oxidative stress. Finally, N-acetyl-L-aspartic acid is a predominant neuronal metabolite involved in myelin lipid production and mitochondrial energy production. While there is no prior direct evidence of its effects in sepsis, its derivative N-acetyl-L-aspartyl-L-glutamate (NAAG) has been shown to increase BBB permeability, a common occurrence under septic conditions[68]. Although further validation is required, our novel cross-compartment approach has yielded a list of strong candidates of clinically-relevant, mechanistically supported biomarker candidates and a framework for discovery that will accelerate early diagnostic efforts in SE.

We reanalyzed core comparisons using our high-confidence, targeted-only metabolomics data to evaluate convergence with findings from the comprehensive dataset. We observed a high level of convergence between the two datasets in cerebellar tissue. Slight differences in the targeted-only dataset emphasized redox balance, mitochondrial energetics, and amino acid metabolism, while signals related to lipid signaling and nucleotide repair functions prominent in the untargeted data were reduced. This likely reflects a stronger

representation of oxidative stress and energy metabolism metabolites in the targeted metabolomics panel, which were preserved even under the more restrictive inclusion criteria. In contrast, plasma results illustrated a decidedly lower consistency between datasets, likely attributable to a reduced overlap in the targeted panel and greater biological heterogeneity relative to cerebellum. Collectively, this reanalysis reinforces the validity of our core conclusions and supports the reliability of our novel comprehensive profiling strategy, while clarifying the distinct contributions of our targeted and untargeted metabolomic approaches.

This study provides the first comprehensive characterization of metabolic alterations in sepsis-associated cerebellar injury and demonstrates the therapeutic potential of MSC-sEVs in mitigating these effects. We propose that their benefits may be mediated through miRNA and protein cargo. In parallel, we identify distinct plasma metabolites with strong promise as biomarkers of sepsis-associated CNS injury, supporting efforts towards earlier diagnosis. Future work is necessary to define the specific contributions of individual MSC-sEV cargo components experimentally. Clarifying the functional roles of MSC-sEV cargo will be essential for understanding the mechanisms by which this treatment exerts its effects. Such insights will advance the development of MSC-sEV-based therapies and support the refinement of targeted interventions for sepsis-related CNS injury. Further, future work is required to validate the diagnostic utility of the identified biomarker candidate metabolites in clinical diagnostic panels. In total, the results of this study establish a foundation for mechanistic and translational advancements in sepsis-associated CNS injury by defining cerebellar metabolic disruptions caused by sepsis, demonstrating the therapeutic impact of MSC-sEV treatment in reversing these disruptions, providing correlational support for future causal investigations into MSC-sEV-based mechanisms of action, and identifying biomarker candidates to aid in early detection and improved clinical management of sepsis.

Limitations

We employed a well-established cecal slurry model of acute murine sepsis with strong construct validity designed to closely approximate key features of human sepsis. A key limitation of this model is the omission of clinical standard-of-care interventions, including antibiotic administration and IV fluid resuscitation. While it may impact the translatability of our findings, this omission was made intentionally to avoid confounding the therapeutic effects of MSC-derived sEVs. Future studies will incorporate standard-of-care analogs to better model real-world clinical conditions.

We also acknowledge limitations inherent to using using putative metabolite annotations based on spectral matching from LC-MS/MS fragmentation databases. To ensure transparency, we reported annotation confidence levels in the Results section and figures. We also performed parallel analyses of all core comparisons using only high-confidence targeted metabolomics data to validate our comprehensive approach findings, including those results in the supplemental materials. For detailed criteria regarding annotation confidence levels and field standards, we refer readers to the framework proposed by Schymanski et al[25].

CONFLICTS OF INTEREST

The authors have no conflicts of interest to declare.

ACKNOWLEDGEMENTS

The research reported in this manuscript was supported by NINDS (1R21NS135088 awarded to IK). We thank Dr. Amrita Cheema, Dr. Shivani Bansal, and Meth Jayatilake from Georgetown University Medical School Lombardi Comprehensive Cancer Center for mass spectrometry services and interpretation support. We thank Dr. John W. Ludlow from Zen-Bio Inc. for providing us with electron microscopy image and protein characterization of MSC-derived sEVs. We thank Dr. Sean Taylor and Research Scientific Computing at Seattle

Children's Research Institute for training and support with the HPC and bioinformatic analyses. We thank Christina Corbaci for graphic illustration design and support. We also thank Dr. Kritika Bhalla, Julian Naizaque, Dr. Alejandro Parga-Becerra, Dr. Emma Parkins, and Olivia Santiago from the Gallo Lab in the Norcliffe Center for Integrative Brain Research at Seattle Children's Research Institute for their input on drafts of this manuscript.

REFERENCES

1. Rudd KE*, et al.* Global, regional, and national sepsis incidence and mortality, 1990–2017: analysis for the Global Burden of Disease Study. *The Lancet* **395**, 200-211 (2020).

2. Bladon S*, et al.* Rapid systematic review on risks and outcomes of sepsis: the influence of risk factors associated with health inequalities. *International Journal for Equity in Health* **23**, 34 (2024).

3. van der Poll T, Shankar-Hari M, Wiersinga WJ. The immunology of sepsis. *Immunity* **54**, 2450-2464 (2021).

4. Aslankoc R, Savran M, Ozmen O, Asci S. Hippocampus and cerebellum damage in sepsis induced by lipopolysaccharide in aged rats-Pregabalin can prevent damage. *Biomedicine & Pharmacotherapy* **108**, 1384-1392 (2018).

5. Koutroulis I*, et al.* Mesenchymal stem cell-derived small extracellular vesicles alleviate the immunometabolic dysfunction in murine septic encephalopathy. *iScience*, 110573 (2024).

6. Harbeson D, Francis F, Bao W, Amenyogbe NA, Kollmann TR. Energy demands of early life drive a disease tolerant phenotype and dictate outcome in neonatal bacterial sepsis. *Frontiers in Immunology* **9**, 408524 (2018).

7. Fujishima S*, et al.* Demographics, treatments, and outcomes of acute respiratory distress syndrome: the focused outcomes research in emergency care in acute respiratory distress syndrome, sepsis, and trauma (FORECAST) study. *Shock* **53**, 544-549 (2020).

8. Hirasawa H, Oda S, Nakamura M. Blood glucose control in patients with severe sepsis and septic shock. *World journal of gastroenterology: WJG* **15**, 4132 (2009).

9. Gofton TE, Young GB. Sepsis-associated encephalopathy. *Nature Reviews Neurology* **8**, 557-566 (2012).

10. Singer M. The new sepsis consensus definitions (Sepsis-3): the good, the not-so-bad, and the actually-quite-pretty. *Intensive Care Med* **42**, 2027-2029 (2016).

11. Li P, Jiao J, Gao G, Prabhakar BS. Control of mitochondrial activity by miRNAs. *Journal of cellular biochemistry* **113**, 1104-1110 (2012).

12. De Melo P*, et al.* Macrophage-derived microRNA-21 drives overwhelming glycolytic and inflammatory response during sepsis via repression of the PGE2/IL-10 axis. *The Journal of Immunology* **207**, 902-912 (2021).

13. Liu Y*, et al.* Acute downregulation of miR-199a attenuates sepsis-induced acute lung injury by targeting SIRT1. *American Journal of Physiology-Cell Physiology* **314**, C449-C455 (2018).

14. Li J, Donath S, Li Y, Qin D, Prabhakar BS, Li P. miR-30 regulates mitochondrial fission through targeting p53 and the dynamin-related protein-1 pathway. *PLoS genetics* **6**, e1000795 (2010).

15. Jiang S. A regulator of metabolic reprogramming: MicroRNA Let-7. *Translational oncology* **12**, 1005-1013 (2019).

16. Karbiener M*, et al.* MicroRNA-26 family is required for human adipogenesis and drives characteristics of brown adipocytes. *Stem cells* **32**, 1578-1590 (2014).

17. Christian P, Su Q. MicroRNA regulation of mitochondrial and ER stress signaling pathways: implications for lipoprotein metabolism in metabolic syndrome. *American Journal of Physiology-Endocrinology and Metabolism* **307**, E729-E737 (2014).

18. Dunn WB, Broadhurst DI, Atherton HJ, Goodacre R, Griffin JL. Systems level studies of mammalian metabolomes: the roles of mass spectrometry and nuclear magnetic resonance spectroscopy. *Chem Soc Rev* **40**, 387-426 (2011).

19. Vinayavekhin N, Homan EA, Saghatelian A. Exploring Disease through Metabolomics. *ACS Chemical Biology* **5**, 91-103 (2010).

20. Jaurila H*, et al.* 1H NMR based metabolomics in human sepsis and healthy serum. *Metabolites* **10**, 70 (2020).

21. Patti GJ, Yanes O, Siuzdak G. Metabolomics: the apogee of the omics trilogy. *NATURE REVIEWS*| *MOLECULAR CELL BIOLOGY* **13**, 263 (2012).

22. Rincon JC, Efron PA, Moldawer LL, Larson SD. Cecal Slurry Injection in Neonatal and Adult Mice. In: *Sepsis: Methods and Protocols* (ed Walker WE). Springer US (2021).

23. Lewis AJ, Seymour CW, Rosengart MR. Current Murine Models of Sepsis. *Surg Infect (Larchmt)* **17**, 385-393 (2016).

24. Shrum B*, et al.* A robust scoring system to evaluate sepsis severity in an animal model. *BMC Research Notes* **7**, 1-15 (2014).

25. Schymanski EL*, et al.* Identifying Small Molecules via High Resolution Mass Spectrometry: Communicating Confidence. *Environmental Science & Technology* **48**, 2097-2098 (2014).

26. Pang Z*, et al.* MetaboAnalyst 6.0: towards a unified platform for metabolomics data processing, analysis and interpretation. *Nucleic Acids Research* **52**, W398-W406 (2024).

27. Pang Z*, et al.* MetaboAnalystR 4.0: a unified LC-MS workflow for global metabolomics. *Nature Communications* **15**, 3675 (2024).

28. Krämer A, Green J, Pollard Jr J, Tugendreich S. Causal analysis approaches in ingenuity pathway analysis. *Bioinformatics* **30**, 523-530 (2014).

29. Çorbacıoğlu Ş K, Aksel G. Receiver operating characteristic curve analysis in diagnostic accuracy studies: A guide to interpreting the area under the curve value. *Turk J Emerg Med* **23**, 195-198 (2023).

30. Chandel NS. Nucleotide metabolism. *Cold Spring Harbor Perspectives in Biology* **13**, a040592 (2021).

31. Kim HS*, et al.* Proteomic analysis of microvesicles derived from human mesenchymal stem cells. *J Proteome Res* **11**, 839-849 (2012).

32. Lizano P*, et al.* The valosin-containing protein is a novel mediator of mitochondrial respiration and cell survival in the heart in vivo. *Scientific reports* **7**, 46324 (2017).

33. Leoni G, Nusrat A. Annexin A1: shifting the balance towards resolution and repair. *Biol Chem* **397**, 971-979 (2016).

34. Purvis GSD, Solito E, Thiemermann C. Annexin-A1: Therapeutic Potential in Microvascular Disease. *Frontiers in Immunology* **Volume 10 - 2019**, (2019).

35. Adibhatla RM, Hatcher JF, Dempsey RJ. Cytidine-5'-diphosphocholine affects CTP-phosphocholine cytidylyltransferase and lyso-phosphatidylcholine after transient brain ischemia. *J Neurosci Res* **76**, 390-396 (2004).

36. Wexler O*, et al.* Methionine Metabolites in Patients With Sepsis. *Journal of Intensive Care Medicine* **33**, 37-47 (2018).

37. Man J, Zhang X. CUEDC2: an emerging key player in inflammation and tumorigenesis. *Protein Cell* **2**, 699-703 (2011).

38. Earley ZM*, et al.* GATA4 controls regionalization of tissue immunity and commensal-driven immunopathology. *Immunity* **56**, 43-57.e10 (2023).

39. Wang S*, et al.* Role of extracellular microRNA-146a-5p in host innate immunity and bacterial sepsis. *Iscience* **24**, (2021).

40. González-López P*, et al.* Role of miR-15a-5p and miR-199a-3p in the inflammatory pathway regulated by NF-κB in experimental and human atherosclerosis. *Clin Transl Med* **13**, e1363 (2023).

41. Vander Heiden MG, Cantley LC, Thompson CB. Understanding the Warburg effect: the metabolic requirements of cell proliferation. *science* **324**, 1029-1033 (2009).

42. Sun J*, et al.* Mitochondria in Sepsis-Induced AKI. *J Am Soc Nephrol* **30**, 1151-1161 (2019).

43. Cantó C*, et al.* AMPK regulates energy expenditure by modulating NAD+ metabolism and SIRT1 activity. *Nature* **458**, 1056-1060 (2009).

44. Ricquier D. Respiration uncoupling and metabolism in the control of energy expenditure. *Proceedings of the Nutrition Society* **64**, 47-52 (2005).

45. Harada H*, et al.* The Akt/mTOR pathway assures the synthesis of HIF-1α protein in a glucose-and reoxygenation-dependent manner in irradiated tumors. *Journal of Biological Chemistry* **284**, 5332-5342 (2009).

46. Laughner E, Taghavi P, Chiles K, Mahon PC, Semenza GL. HER2 (neu) signaling increases the rate of hypoxia-inducible factor 1α (HIF-1α) synthesis: novel mechanism for HIF-1-mediated vascular endothelial growth factor expression. *Molecular and cellular biology* **21**, 3995-4004 (2001).

47. Zhou J, Callapina M, Goodall GJ, Brüne B. Functional integrity of nuclear factor κB, phosphatidylinositol 3′-kinase, and mitogen-activated protein kinase signaling allows tumor necrosis factor α-evoked Bcl-2 expression to provoke internal ribosome entry site-dependent translation of hypoxia-inducible factor 1α. *Cancer research* **64**, 9041-9048 (2004).

48. Galván-Peña S*, et al.* Malonylation of GAPDH is an inflammatory signal in macrophages. *Nature Communications* **10**, 338 (2019).

49. Wernly B, Lichtenauer M, Hoppe UC, Jung C. Hyperglycemia in septic patients: an essential stress survival response in all, a robust marker for risk stratification in some, to be messed with in none. *J Thorac Dis* **8**, E621-624 (2016).

50. Rivas AM, Nugent K. Hyperglycemia, Insulin, and Insulin Resistance in Sepsis. *The American Journal of the Medical Sciences* **361**, 297-302 (2021).

51. Lazar A-G, Vlad M-L, Manea A, Simionescu M, Manea S-A. Activated Histone Acetyltransferase p300/CBP-Related Signalling Pathways Mediate Up-Regulation of NADPH Oxidase, Inflammation, and Fibrosis in Diabetic Kidney. *Antioxidants* **10**, 1356 (2021).

52. Gandhirajan A, Roychowdhury S, Vachharajani V. Sirtuins and Sepsis: Cross Talk between Redox and Epigenetic Pathways. *Antioxidants (Basel)* **11**, (2021).

53. Wald EL, Badke CM, Hintz LK, Spewak M, Sanchez-Pinto LN. Vitamin therapy in sepsis. *Pediatric Research* **91**, 328-336 (2022).

54. Fink MP. Cytopathic Hypoxia: Mitochondrial Dysfunction as Mechanism Contributing to Organ Dysfunction in Sepsis. *Critical Care Clinics* **17**, 219-237 (2001).

55. Zhang X*, et al.* Desuccinylation of TBK1 by SIRT5 regulates inflammatory response of macrophages in sepsis. *Cell Reports* **43**, (2024).

56. Lennicke C, Cochemé HM. Redox metabolism: ROS as specific molecular regulators of cell signaling and function. *Molecular Cell* **81**, 3691-3707 (2021).

57. Hyun DH. Insights into the New Cancer Therapy through Redox Homeostasis and Metabolic Shifts. *Cancers (Basel)* **12**, (2020).

58. Singh CK, Chhabra G, Ndiaye MA, Garcia-Peterson LM, Mack NJ, Ahmad N. The Role of Sirtuins in Antioxidant and Redox Signaling. *Antioxid Redox Signal* **28**, 643-661 (2018).

59. Zhu C*, et al.* Multiple Roles of SIRT2 in Regulating Physiological and Pathological Signal Transduction. *Genet Res (Camb)* **2022**, 9282484 (2022).

60. Averill-Bates DA. The antioxidant glutathione. *Vitam Horm* **121**, 109-141 (2023).

61. Ortega-Prieto P*, et al.* O-GlcNAc transferase acts as a critical nutritional node for the control of liver homeostasis. *JHEP Rep* **6**, 100878 (2024).

62. Chen PH*, et al.* Glycosylation of KEAP1 links nutrient sensing to redox stress signaling. *The EMBO Journal* **36**, 2233-2250 (2017).

63. Mierzchała-Pasierb M*, et al.* An analysis of urine and serum amino acids in critically ill patients upon admission by means of targeted LC–MS/MS: a preliminary study. *Scientific Reports* **11**, 19977 (2021).

64. Soulet D, Rivest S. Polyamines play a critical role in the control of the innate immune response in the mouse central nervous system. *Journal of Cell Biology* **162**, 257-268 (2003).

65. Chen C, Meng X, Zhu Y, Zhang J, Wang R. Early Identification of Serum Biomarkers and Pathways of Sepsis Through GC-MS-Based Metabolomics Analysis. *FBL* **28**, (2023).

66. Izquierdo-Garcia JL*, et al.* Identification of novel metabolomic biomarkers in an experimental model of septic acute kidney injury. *Am J Physiol Renal Physiol* **316**, F54-f62 (2019).

67. Wang Y*, et al.* Prognostic impact of blood urea nitrogen to albumin ratio on patients with sepsis: a retrospective cohort study. *Scientific Reports* **13**, 10013 (2023).

68. Barichello T, Generoso JS, Collodel A, Petronilho F, Dal-Pizzol F. The blood-brain barrier dysfunction in sepsis. *Tissue Barriers* **9**, 1840912 (2021).

69. Gavins FN, Hickey MJ. Annexin A1 and the regulation of innate and adaptive immunity. *Frontiers in immunology* **3**, 354 (2012).

70. Tuerdi B, Zuo L, Ma Y, Wang K. Downregulation of miR-155 attenuates sepsis-induced acute lung injury by targeting SIRT1. *International journal of clinical and experimental pathology* **11**, 4483 (2018).

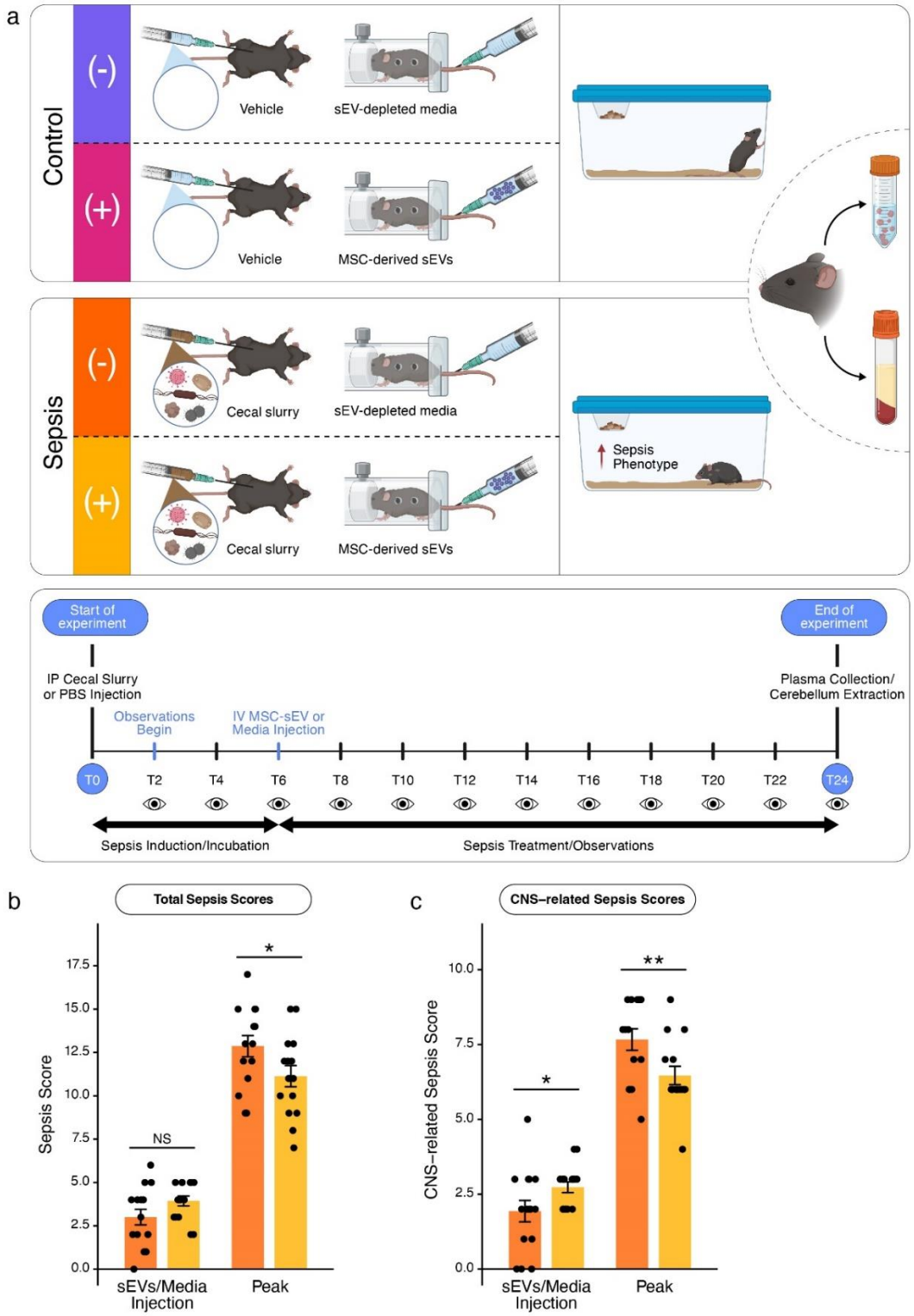

Figure 1. **Overview of experimental design and clinical scoring**. (**a**) Schematic and experimental timeline of the cecal slurry model of sepsis. This panel outlines the nature of the four experimental groups, their treatments, and the timeline on which sepsis is inducted and observed followed by sample collection. Schematic created in BioRender. Crawford, D. (2025) https://BioRender.com/y63q355. (**b**) Group means and variability in average total clinical sepsis scores for untreated, Sepsis (-), and treated, Sepsis (+), animals at the time of treatment administration and at peak observed illness. (**c**) Group average scores based on a subset of total clinical sepsis scores which reflects a CNS-specific phenotypes. Control groups are not shown in the plots, as scores remained negligible (≤ 0.5) across both measures at both timepoints. Data represented as mean ± SEM, Independent samples t-test. NS: non-significant, * denotes $p \leq 0.05$, ** denotes p-value ≤ 0.01.

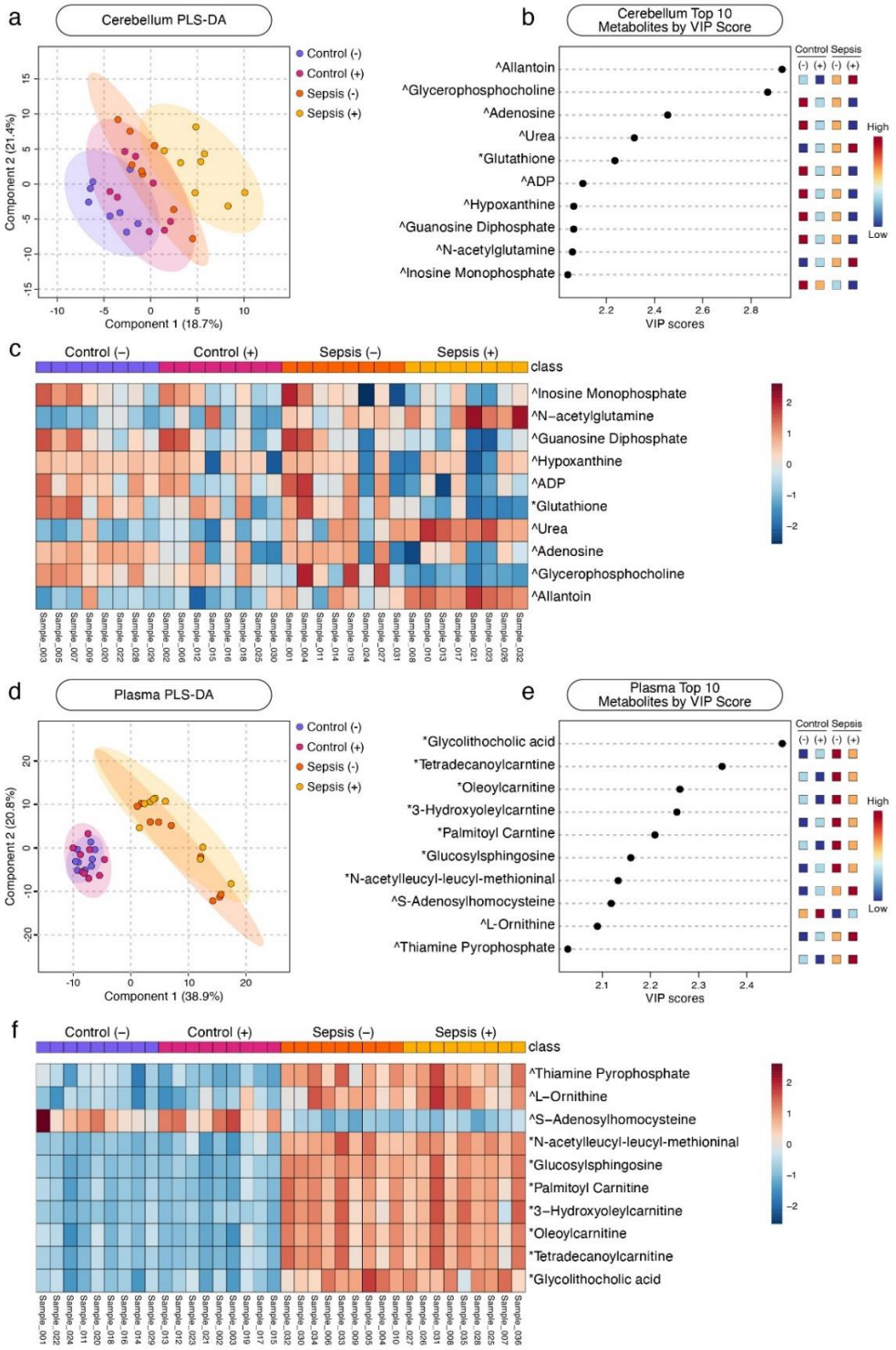

Figure 2. Multivariate analysis identifies discriminatory metabolite profiles in cerebellar tissue and plasma. PLS-DA plots of cerebellum (**a**) and plasma (**d**) samples where the horizontal and vertical axes represent Components 1 and 2, respectively. These components capture directions in the data that maximize covariance between metabolite profiles and group labels where Component 1 explains the strongest class-related pattern and Component 2 the next most discriminative, orthogonal pattern. Ellipses represent the 95% confidence interval. **b**) Variable Importance in Projection (VIP) score graphs for cerebellum (**b**) and plasma (**e**) samples display the top 10 metabolites contributing to group separation along Component 1, with VIP scores reflecting each metabolite's contribution to the model's power to discriminate samples by group. Heatmaps of the top 10 metabolites by VIP score from cerebellum (**c**) and plasma (**f**) PLS-DAs showing relative peak intensities across each sample and grouped by experimental condition. Caret symbols (^) denote a Level 1-2 confidence identification from core facility panel confirmed by reference standard; Asterisks (*) denote a putatively annotated feature from LC-MS/MS fragmentation matches using the NIST MS Search software, earning Level 3+ identification confidence[25].

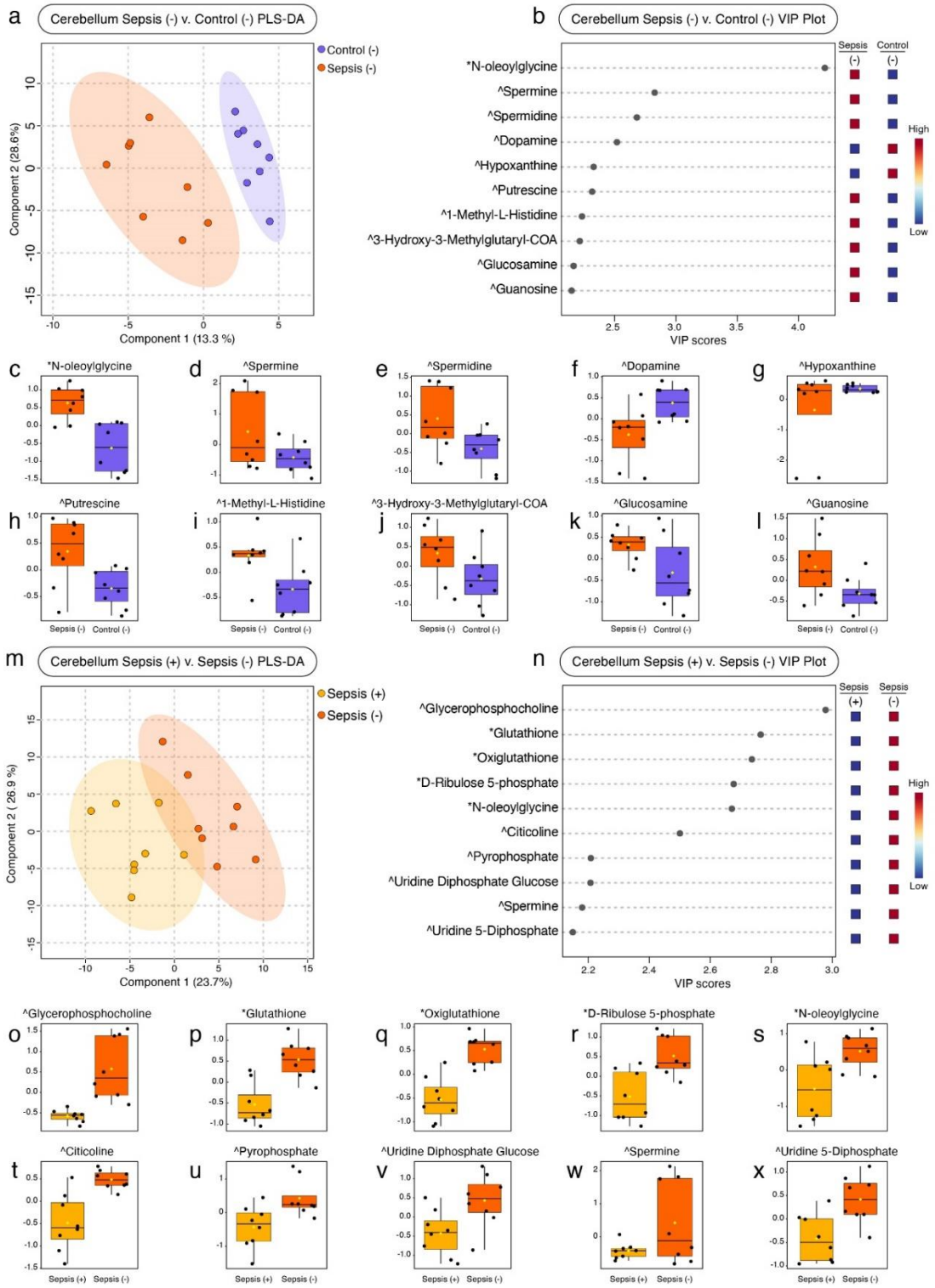

Figure 3. **Variable isolating group comparisons in cerebellar metabolite profiles reveal effects of disease state and treatment**. This figure presents PLS-DA-derived discriminant features from cerebellar samples, restricted to two pairwise group comparisons. Panels **a-l** illustrate the comparison between untreated septic animals and healthy control, Sepsis (-) v. Control (-), isolating the metabolic profiles associated with disease state. Panels **m-x** display data from the Sepsis (+) v. Sepsis (-) comparison, capturing effects related to the effect of MSC-sEV treatment under septic conditions. (**a, m**) PLS-DA model illustration showing sample clustering along the first two components with 95% confidence ellipses for each group. (**b, n**) VIP score plots showing the top 10 metabolites contributing to Component 1 and driving separation by experimental condition. (**c-l, o-x**) Box plots for each of the top 10 metabolites by VIP score in their respective comparisons, depicting average relative peak intensity by group. Caret symbols(^) denote a Level 1-2 confidence identification from core facility panel confirmed by reference standard; Asterisks (*) denote a putatively annotated feature from LC-MS/MS fragmentation matches using the NIST MS Search software, earning Level 3+ identification confidence[25].

Figure 4. **Canonical pathway activity and upstream regulator predictions in cerebellar tissue across disease and treatment comparisons**. Panels **a-c** focus on the disease state comparison, Sepsis (-) v. Control (-), while panels **d-f** focus on the treatment comparison, Sepsis (+) v. Sepsis (-). (**a,d**) Canonical pathway activity showing all pathways predicted to be affected as determined by cerebellar metabolite intensities. Pathways are grouped by their biological function (y-axis) and plotted against their alteration significance ($-\log_{10}$[p-value]; x-axis). Bubble size reflects the proportion of the measured metabolites relative to total known pathway metabolite profile, while bubble color represents the predicted activation direction and intensity (orange = predicted up-regulation, blue = predicted down-regulation). (**b,e**) Top 20 canonical pathways as ranked by Pathway Impact score. (**c,f**) Top 10 predicted upstream regulators influenced by each condition based on metabolite representation. Each regulator (y-axis) is displayed as a bar with a length representing its $-\log_{10}$(p-value of overlap; x-axis) and is colored according to its predicted activation direction and intensity.

	Sepsis (-) v. Control (-)			Sepsis (+) v. Sepsis (-)		
Rank	Pathway Name	Biological Function Category	Impact Score	Pathway Name	Biological Function Category	Impact Score
1	Nucleotide catabolism	Metabolism	+0.83	Transport of bile salts & organic acids, metal ions & amine compounds	Transport of Small Molecules	+0.76
2	Transport of bile salts & organic acids, metal ions & amine compunds	Transport of Small Molecules	-0.76	Superpathway of Citrulline Metabolism	Biosynthesis	-0.75
3	Superpathway of Citruline Metabolism	Biosynthesis	+0.75	Urea Cycle	Metabolism, Degradation/Utilization/Assimilation	-0.75
4	Urea Cycle	Metabolism, Degradation/Utilization/Assimilation	+0.75	Arginine Biosynthesis IV	Biosynthesis	-0.74
5	Arginine Biosynthesis IV	Metabolism	+0.74	Citric acid cycle (TCA cycle)	Metabolism	+0.74
6	Citric acid cycle (TCA cycle)	Metabolism	-0.74	Interconversion of nucleotide di- and triphosphates	Metabolism	+0.74
7	Interconversion of nucleotide di- and triphospates	Metabolism	-0.74	Nucleotide salvage	Metabolism	-0.73
8	Citrulline-Nitric Oxide Cycle	Biosynthesis, Degradation/Utilization/Assimilation	+0.73	Citruline-Nitric Oxide Cycle	Biosynthesis, Degredation/Utilization/Assimilation	-0.73
9	Sirtuin Signaling Pathway	Intracellular & Secondary Messenger Signaling, Transcriptional Regulation	-0.73	Sirtuin Signaling Pathway	Intracellular & Secondary Messenger Signaling, Transcriptional Regulation	-0.73
10	Mismatch Repair	Autophagy, DNA Repair	+0.73	Mismatch Repair	Autophagy, DNA Repair	-0.73
11	Sulfur amino acid metabolism	Metabolism	-0.72	Sulfur amino acid metabolism	Metabolism	+0.72
12	Metabolism of water-soluble vitamins and cofactors	Metabolism	+0.72	Metabolism of water- soluble vitamins and cofactors	Metabolism	+0.72
13	Choline catabolism	Metabolism	-0.71	Choline catabolism	Metabolism	+0.72
14	Purine Nucleotides De Novo Biosynthesis II	Biosynthesis	+0.69	Purine Nucleotides De Novo Biosynthesis II	Biosynthesis	-0.69
15	Glutamate and glutamine metabolism	Metabolism	-0.68	Glutamate and glutamine metabolism	Metabolism	+0.68
16	Nucleotide biosynthesis	Metabolism	-0.68	Nucleotide biosynthesis	Metabolism	+0.68
17	Pyruvate metabolism	Metabolism	-0.67	Pyruvate metabolism	Metabolism	+0.67
18	Superpathway of Methionine Degradation	Degradation/Utilization/Assimilation	+0.67	Superpathway of Methionine Degradation	Degradation/Utilization/Assimilation	-0.67
19	Flavin Biosynthesis IV (Mammalian)	Biosynthesis	+0.67	Flavin Biosynthesis IV (Mammalian)	Biosynthesis	-0.67
20	Cytosolic sensors of pathogen-associated DNA	Immune System	+0.67	Glucogenesis I	Biosynthesis	-0.67

Table 1. Top 20 canonical pathways altered in cerebellar tissue by disease and treatment conditions. Listed in this table are the top 20 canonical pathways altered from between disease state, Sepsis (-) v. Control (-), and treatment, Sepsis (+) v. Sepsis (-), comparisons as determined by Pathway Impact score. This table identifies the individual pathway names, biological function category to which each pathway belongs, and the Pathway Impact score for each pathway. Direction of regulation is denoted by sign on impact score: positive (+) for predicted up-regulation, negative (-) for predicted down-regulation.

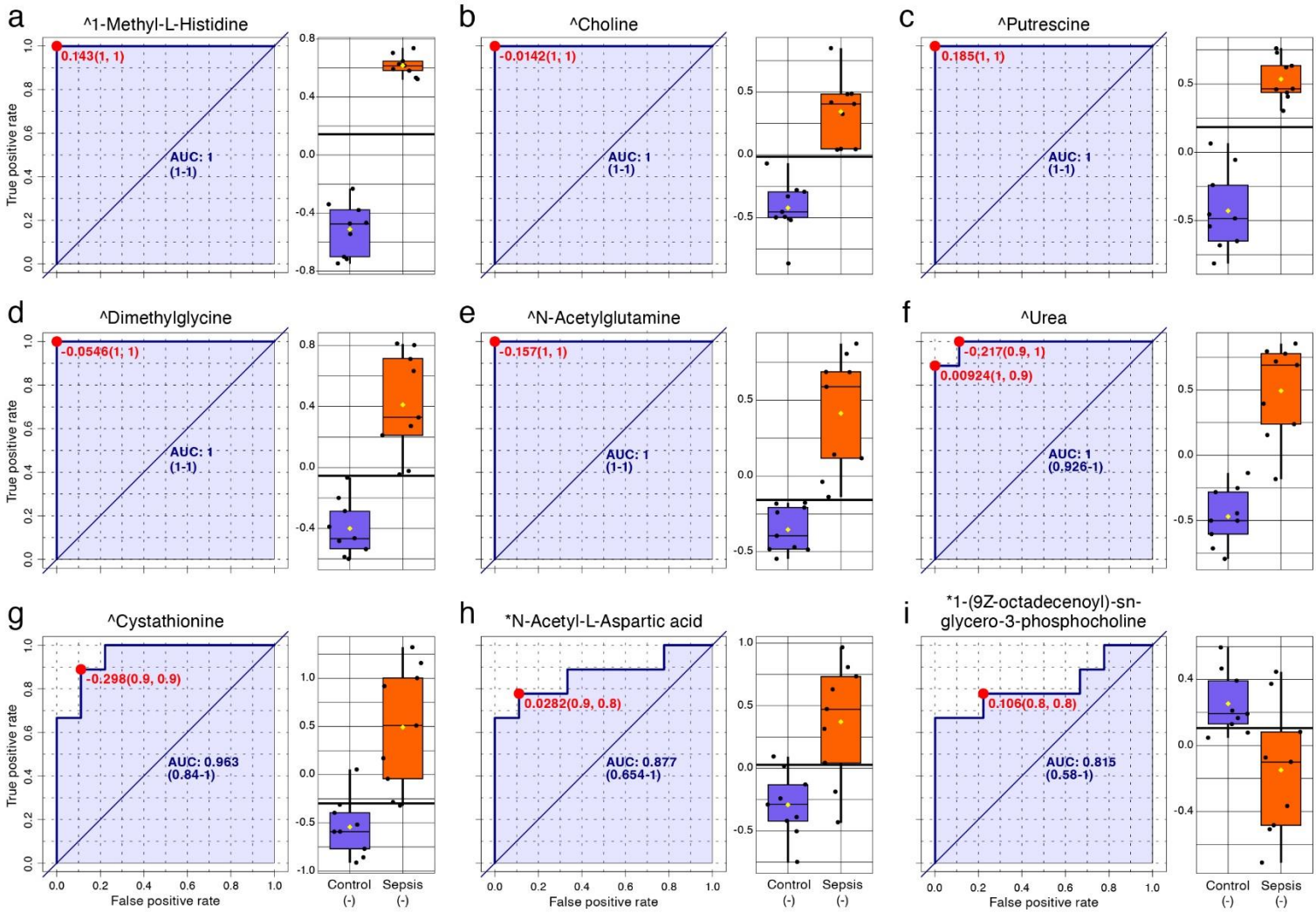

Figure 5. **Overlapping biomarker candidates with high diagnostic performance in both cerebellum and plasma.** This figure displays all nine metabolite features with strong diagnostic potential (AUC ≥ 0.8) that were altered in both cerebellar and plasma samples considering the disease state comparison, Sepsis (-) v. Control (-). Panels **a-i** display receiver operating characteristic (ROC) curves for each overlapping metabolite candidate, with AUC values shown to reflect classification performance. Box plots are displayed to the right of each metabolite's ROC curve, illustrating the relative average concentrations of each metabolite by condition. Where known, the best diagnostic threshold is displayed by a black horizontal line on the box plots. Caret symbols (^) denote a Level 1-2 confidence identification from core facility panel confirmed by reference standard; Asterisks (*) denote a putatively annotated feature from LC-MS/MS fragmentation matches using the NIST MS Search software, earning Level 3+ identification confidence[25].

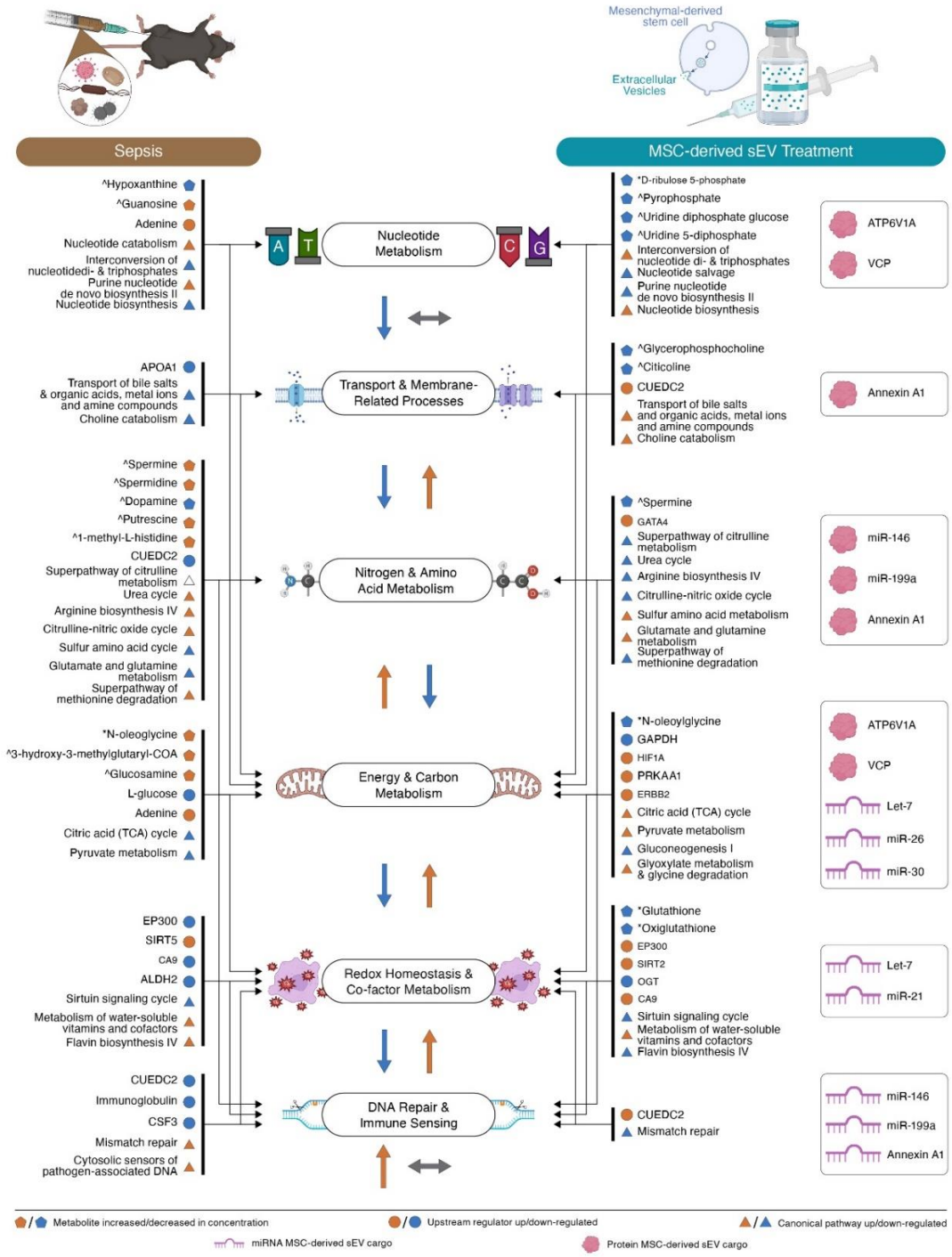

Figure 6. **Integrated summary of comprehensive metabolic profiles (including metabolite alterations, predicted canonical pathway and upstream regulator activity) across disease and treatment conditions, alongside potential mechanistic influences of MSC-sEV cargo.** This figure summarizes the affected metabolites, regulatory networks, and pathway-level alterations, illustrated as influences to inferred net biological outcomes. Arrows demonstrate which groups of metabolic profile components are likely to influence which biological outcomes. The **left column** presents changes observed or predicted in the disease state comparison, Sepsis (-) v. Control (-). The **right column** depicts changes associated with the treatment comparison, Sepsis (+) v. Sepsis (-), in addition to the potential MSC-sEV cargo influences the observed changes. Component shape denotes type (pentagon = metabolite, circle = upstream regulator, and triangle = canonical pathway) and color indicates directionality (orange = increase concentration or predicted up-regulation, blue = decreased concentration or predicted down-regulation). Large arrows under each biological outcome indicates the predicted net effect on that function. All metabolite concentrations changes were directly observed, while pathway and upstream regulator activation state are predicted based on metabolite data. Caret symbols (^) denote a Level 1-2 confidence identification from core facility panel confirmed by reference standard; Asterisks (*) denote a putatively annotated feature from LC-MS/MS fragmentation matches using the NIST MS Search software, earning Level 3+ identification confidence[25].

MSC-sEV Cargo	Evidenced Function	Proposed Mechanism	Supporting Evidence from Metabolomics Analyses	Biological Function Category
ATP6V1A	Regulation of ATP-generating pathways[31]	Supports ATP generation via mitochondrial membrane potential regulation	↑ Nucleotide interconversion	Nucleotide Metabolism
			↑ TCA Cycle/Pyruvate metabolism	
			↑ Nucleotide biosynthesis	Energy & Carbon Metabolism
			↓ D-ribulose 5-phosphate	
Valosin-containing protein (VCP)	Regulation of ATP-generating pathway[31, 32]	Enhances mitochondrial turnover and supports energy metabolism under stress	↑ Nucleotide interconversion	Nucleotide Metabolism
			↑ TCA Cycle/Pyruvate metabolism	
	Supports mitochondrial respiration and stress recovery[32]		↑ Nucleotide biosynthesis	Energy & Carbon Metabolism
			↓ D-ribulose 5-phosphate	
Annexin A1	Modulates innate and adaptive immunity[69]	Resolves inflammation	↑ CUEDC2	Transport & Membrane Related Processes
		Promotes repair	↑ Choline catabolism	
	Reduces leukocyte infiltration and inflammation[33, 69]		↓ Glycerophosphocholine	DNA Repair & Immune Sensing
		Stabilizes membrane related signaling	↓ Citicoline	
miR-146	Suppresses pro-inflammatory cytokines TNFα and IL-6[39]	Dampens inflammatory signaling and restores regulatory immune control	↑ CUEDC2	Nitrogen & Amino Acid Metabolism
			↓ N-oleoylglycine	
	Restores innate immune regulation[39]		↓ GAPDH	DNA Repair & Immune Sensing
			↓ Mismatch repair	
miR-199a	Suppresses NF-κB signaling and pro- inflammatory cytokines TNFα and IL-6[13, 40]	Modulates SIRT signaling to reduce oxidative stress and promote redox balance	↑ SIRT2	Nitrogen & Amino Acid Metabolism
	Regulates SIRT1 [13,70]		↑ EP300	DNA Repair & Immune Sensing
miR-30	Directly controls mitochondrial dynamics and OXPHOS[14]	Enhances mitochondrial integrity and OXPHOS by regulating fission/fusion balance	↑ TCA cycle	Energy & Carbon Metabolism
			↑ Pyruvate metabolism	
	Alters pathways to maintain lipid metabolism homeostasis[32]		↓ N-oleoylglycine	
	Regulates mitochondrial fission via p53/DRP1[14]		↑ PRKAA1	
			↑ ERBB2	
Let-7	Directly controls mitochondrial dynamics and OXPHOS[15]	Supports oxidative metabolism and mitochondrial homeostasis	↑ Glutathione metabolism	Energy & Carbon Metabolism
	Supports mitochondrial function and metabolic reprogramming[15]		↑ CA9	
	Reduces inflammation[15]	Enhances glutathione synthesis	↑ Sulfur amino acid metabolism	Redox homeostasis & Co-factor Metabolism
			↓ Glutathione	
miR-26	Directly controls mitochondrial dynamics and OXPHOS[16]	Enhances mitochondrial biogenesis and energy pathway activation	↑ TCA cycle	Energy & Carbon Metabolism
	Promotes adipogenesis[16]		↑ Pyruvate metabolism	
			↑ SIRT2	
	Enhances OXPHOS and energy expenditure[16]		↑ Glyoxylate metabolism	
miR-21	Overexpressed in neutrophils and macrophages in sepsis[12]	Activates antioxidant gene expression and reduces inflammatory signaling	↑ EP300	Redox Homeostasis & Co-factor Metabolism
	Controls inflammation by repressing PGE2/IL-10 axis[12]		↑ CA9	
			↑ Metabolism of water-solublevitamins	
	Promotes glycolysis and antioxidant response[12]		↓ Glutathione	

Table 2. **Summary of established MSC-sEV miRNA and protein bioactive cargo, with proposed mechanisms of influence in treated septic animals.** For each cargo, known biological functions are listed alongside a proposed mechanism by which it may affect physiological processes in septic animals given MSC-sEV treatment. Supporting correlational evidence from our metabolomics data, by way of observed changes in metabolites or predicted alterations to upstream regulators and/or canonical pathways, is included along with the corresponding biological function category as previously defined in **Figure 6**.